PHYSICAL REVIEW D **93,** 044046 (2016)

Energetics and phasing of nonprecessing spinning coalescing black hole binaries

Alessandro Nagar,[1] Thibault Damour,[1] Christian Reisswig,[2] and Denis Pollney[3]

[1]*Institut des Hautes Etudes Scientifiques, 91440 Bures-sur-Yvette, France*
[2]*Department of Mathematics, Rhodes University, 6140 Grahamstown, South Africa*
[3]*Theoretical Astrophysics Including Relativity, California Institute of Technology, Pasadena, California 91125, USA*

(Received 28 June 2015; published 17 February 2016)

We present an improved numerical relativity (NR) calibration of the new effective-one-body (EOB) model for coalescing nonprecessing spinning black hole binaries recently introduced by Damour and Nagar [Phys. Rev. D 90, 044018 (2014)]. We do so by comparing the EOB predictions to both the phasing and the energetics provided by two independent sets of NR data covering mass ratios $1 \leq q \leq 9.989$ and dimensionless spin range $-0.95 \leq \chi \leq +0.994$. One set of data is a subset of the Simulating eXtreme Spacetimes (SXS) catalog of public waveforms; the other set consists of new simulations obtained with the Llama code plus Cauchy characteristic evolution. We present the first systematic computation of the gauge-invariant relation between the binding energy and the total angular momentum, $E_b(j)$, for a large sample of, spin-aligned, SXS and Llama data. The dynamics of the EOB model presented here involves only two free functional parameters, one $[a_6^c(\nu)]$ entering the nonspinning sector, as a 5PN effective correction to the interaction potential, and one $[c_3(\tilde{a}_1, \tilde{a}_2, \nu)]$ in the spinning sector, as an effective next-to-next-to-next-to-leading order correction to the spin-orbit coupling. These parameters are determined [together with a third functional parameter $\Delta t_{\rm NQC}(\chi)$ entering the waveform] by comparing the EOB phasing with the SXS phasing, the consistency of the energetics being checked afterwards. The quality of the analytical model for gravitational wave data analysis purposes is assessed by computing the EOB/NR faithfulness. Over the NR data sample and when varying the total mass between 20 and 200 $M_\odot$ the EOB/NR unfaithfulness (integrated over the NR frequency range) is found to vary between 99.493% and 99.984% with a median value of 99.944%.

DOI: 10.1103/PhysRevD.93.044046

I. INTRODUCTION

The purpose of this paper is to present an improved version of the new spinning effective-one-body (EOB) model introduced in Ref. [1], hereafter Paper I. [For earlier spinning EOB models see [2–13]]. When the mass of the binary varies between 20 and 200 $M_\odot$, our improved model yields, when compared to a large sample of numerical relativity (NR) waveform data, maximal unfaithfulnesses ($\bar{F} \equiv 1 - F$, integrated over the NR frequency range) ranging between 0.00016 and 0.00507, with median value equal to 0.00056. The impatient data-analyst reader will find this information in Figs. 9 and 21 and the text around. The structural elements of our improved EOB model behind such good faithfulnesses are (i) the incorporation of the full 4PN-accurate analytical knowledge of the EOB radial interaction; and (ii) the use of a recently proposed improved ringdown description [14]. The use of the 4PN information obliged us to update the calibration of both the effective 5PN-coefficient a_6^c entering the nonspinning sector, and the effective next-to-next-to-next-to-leading order spin-orbit coupling coefficient c_3 of Paper I.

Here, we restrict attention to the nonprecessing case where the spins are either aligned or antialigned with respect to the orbital angular momentum. The EOB/NR comparisons that are used to gain new information from NR data so as to complete the EOB model are of two kinds: (i) on the one hand, we compare the gravitational wave (GW) *phasing* of the EOB model with 40 state-of-the-art (publicly available [15]) NR waveforms produced by the Caltech-Cornell-CITA Simulating eXtreme Spacetimes (SXS) collaboration with the Spectral Einstein Code (SpEC) code [16–25]; 11 configurations in this sample involve nonspinning binaries, while in the remaining 29 at least one black hole is spinning; (ii) on the other hand we compare the EOB and NR *energetics* through the gauge-invariant relation between energy and angular momentum. To do so, we employ, in addition to the SXS data sets, ten newly performed simulations obtained with the Llama code, as a follow up of our previous work [26].

The paper is organized as follows: in Sec. II we briefly review the origin of the NR data used in this paper, which were obtained with very different codes. In Secs. III–IV we focus on the improved calibration of the nonspinning sector, its phasing and energetics, notably showing the good agreement between energetics when $\mathcal{F}_{r_*} = 0$ for the mass ratio range $1 \leq q \leq 9.989$. In Secs. V-VIwe calibrate the effective spin-orbit parameter c_3 and we assess the quality of this new spinning EOB model by computing both

TABLE I. EOB/NR phasing comparison. The columns report the number of the data sets; the name of the configuration in the SXS catalog; the mass ratio $q = m_1/m_2$; the symmetric mass ratio ν; the dimensionless spins χ_1 and χ_2; the phase difference $\Delta\phi^{\rm EOBNR} \equiv \phi^{\rm EOB} - \phi^{\rm NR}$ computed at NR merger; the NR phase uncertainty at NR merger $\delta\phi^{\rm NR}_{\rm mrg}$ (when available) measured taking the difference between the two highest resolution levels (see text); the maximum value of the unfaithfulness $\bar{F} \equiv 1 - F$ as per Eq. (22). The $\Delta\phi^{\rm EOBNR}$'s in brackets for $\chi_1 = \chi_2 > +0.85$ were obtained using Eq. (21) for $\Delta t^{\rm NQC}(\chi)$.

#	Name	N orbits	q	ν	χ_1	χ_2	$\Delta\phi^{\rm EOBNR}_{\rm mrg}$ [rad]	$\delta\phi^{\rm NR}_{\rm mrg}$ [rad]	$\max(\bar{F})$
1	SXS:BBH:none	14	1	0.25	0.0	0.0	−0.016	…	0.00087
2	SXS:BBH:0066	28	1	0.25	0.0	0.0	+0.010	…	0.00068
3	SXS:BBH:0002	32.42	1	0.25	0.0	0.0	+0.073	0.066	0.00101
4	SXS:BBH:0007	29.09	1.5	0.24	0	0	+0.05	0.018	0.00201
5	SXS:BBH:0169	15.68	2	$0.\bar{2}$	0	0	−0.15	0.02	0.00045
6	SXS:BBH:0030	18.22	3	0.1875	0	0	−0.074	0.087	0.00035
7	SXS:BBH:0167	15.59	4	0.16	0	0	−0.059	0.52	0.00035
8	SXS:BBH:0056	28.81	5	$0.13\bar{8}$	0	0	−0.089	0.44	0.00038
9	SXS:BBH:0166	21.56	6	0.1224	0	0	−0.198	…	0.00037
10	SXS:BBH:0063	25.83	8	0.0987	0	0	−0.453	1.01	0.00292
11	SXS:BBH:0185	24.91	9.98911	0.0827	0	0	−0.0051	0.376	0.00066
12	SXS:BBH:0004	30.19	1	0.25	−0.50	0.0	−0.017	0.068	0.00403
13	SXS:BBH:0005	30.19	1	0.25	+0.50	0.0	+0.08	0.28	0.00052
14	SXS:BBH:0156	12.42	1	0.25	−0.95	−0.95	+0.32	2.17	0.00058
15	SXS:BBH:0159	12.67	1	0.25	−0.90	−0.90	+0.06	0.38	0.00047
16	SXS:BBH:0154	13.24	1	0.25	−0.80	−0.80	+0.11	…	0.00044
17	SXS:BBH:0151	14.48	1	0.25	−0.60	−0.60	−0.049	0.14	0.00042
18	SXS:BBH:0148	15.49	1	0.25	−0.44	−0.44	+0.14	0.72	0.00043
19	SXS:BBH:0149	17.12	1	0.25	−0.20	−0.20	+0.45	0.90	0.00085
20	SXS:BBH:0150	19.82	1	0.25	+0.20	+0.20	+0.94	0.99	0.00275
21	SXS:BBH:0152	22.64	1	0.25	+0.60	+0.60	+0.01	0.36	0.00068
22	SXS:BBH:0155	24.09	1	0.25	+0.80	+0.80	−0.39	0.26	0.00110
23	SXS:BBH:0153	24.49	1	0.25	+0.85	+0.85	+0.06	…	0.00059
24	SXS:BBH:0160	24.83	1	0.25	+0.90	+0.90	+0.41 (+0.41)	0.80	0.00117
25	SXS:BBH:0157	25.15	1	0.25	+0.95	+0.95	+0.37 (+0.83)	1.18	0.00295
26	SXS:BBH:0158	25.27	1	0.25	+0.97	+0.97	+0.37 (+0.49)	1.26	0.00325
27	SXS:BBH:0172	25.35	1	0.25	+0.98	+0.98	+0.99 (+0.46)	2.02	0.00422
28	SXS:BBH:0177	25.40	1	0.25	+0.99	+0.99	+0.22 (+0.48)	0.40	0.00507
29	SXS:BBH:0178	25.43	1	0.25	+0.994	+0.994	+0.24 (+0.23)	−0.53	0.00506
30	SXS:BBH:0013	23.75	1.5	0.24	+0.5	0	+0.31	…	0.00058
31	SXS:BBH:0014	22.63	1.5	0.24	−0.5	0	−0.15	0.15	0.00046
32	SXS:BBH:0162	18.61	2	$0.\bar{2}$	+0.6	0	−0.20	0.71	0.00027
33	SXS:BBH:0036	31.72	3	0.1875	−0.5	0	+0.08	0.065	0.00040
34	SXS:BBH:0031	21.89	3	0.1875	+0.5	0	+0.12	0.034	0.00023
35	SXS:BBH:0047	22.72	3	0.1875	+0.5	+0.5	−0.034	…	0.00030
36	SXS:BBH:0046	14.39	3	0.1875	−0.5	−0.5	+0.36	…	0.00054
37	SXS:BBH:0110	24.24	5	$0.13\bar{8}$	+0.5	0	+0.24	…	0.00016
38	SXS:BBH:0060	23.17	5	$0.13\bar{8}$	−0.5	0	+0.21	0.8	0.00034
39	SXS:BBH:0064	19.16	8	0.0987	−0.5	0	+0.026	0.8	0.00042
40	SXS:BBH:0065	33.97	8	0.0987	+0.5	0	+1.33	−3.0	0.00040

the EOB/NR unfaithfulness and the energetics. In Sec. VII we present a preliminary comparison of our EOB model with that of Buonanno's group [11]. Finally, Sec. VIII presents concluding remarks, future prospects as well as a histogram summarizing the unfaithfulness calculations.

We use geometrized units with $G = c = 1$ and the following notation: $M = m_1 + m_2$, $\mu = m_1 m_2/M$, $\nu = \mu/M$ with the convention that the mass ratio $q \equiv m_1/m_2 \geq 1$.

II. NUMERICAL RELATIVITY DATA

A. Data from the SXS public catalog

We use a sample of 40 simulations from the SXS catalog. We consider either nonspinning or spin-aligned configurations, with mass ratios in the range $1 \leq q \leq 9.989$ and dimensionless spin magnitude $-0.95 \leq \chi \leq +0.994$. In several cases, just one of the two black holes is spinning.

TABLE II. BBH configurations, evolved using the Llama code, used to compute the gauge-invariant relation between energy and angular momentum. From left to right: name of the run, number of orbits up to merger, mass ratio $q \equiv m_1/m_2$, symmetric mass ratio ν, dimensionless spins of the two black holes, (χ_1, χ_2); the initial ADM mass $M^0_{\rm ADM}$; initial total angular momentum $\mathcal{J}^0_{\rm ADM}$.

Name	N orbits	q	ν	χ_1	χ_2	$M^0_{\rm ADM}$	$\mathcal{J}^0_{\rm ADM}$
q1_s0	8.09	1	0.25	0.0	0.0	0.99051968	0.99325600
q2_s0	6.70	2	$0.\bar{2}$	0.0	0.0	0.990898	0.85599600
q1_s-8D10_h96	3.83	1	0.25	−0.8	−0.8	0.989412	0.61736
q1_s-8D10_h1152	3.84	1	0.25	−0.8	−0.8	0.989412	0.61736
q1_s-6D12_h64	8.25	1	0.25	−0.6	−0.6	0.986161	0.7552392
q1_s-6D12_h512	8.23	1	0.25	−0.6	−0.6	0.986161	0.7552392
q1_s-4D10_h64	5.67	1	0.25	−0.4	−0.4	0.990138	0.791588
q1_s-2D10_h64	5.88	1	0.25	−0.2	−0.2	0.989941	0.877499
q1_s-2D10_h512	5.88	1	0.25	−0.2	−0.2	0.989941	0.877499
q1_s2D8_h64	4.93	1	0.25	+0.2	+0.2	0.987658	0.984992
q1_s2D8_h512	4.93	1	0.25	+0.2	+0.2	0.987658	0.984992
q1_s4D8_h64	5.67	1	0.25	+0.4	+0.4	0.987619	1.072176
q1_s6D8_h64	6.38	1	0.25	+0.6	+0.6	0.987649	1.160296
q1_s6D8_h512	6.48	1	0.25	+0.6	+0.6	0.987649	1.160296
q1_s8D8_h64	7.24	1	0.25	+0.8	+0.8	0.987744	1.249296

The complete information about the data we used is listed in Table I. For each run, when it is possible, we add an error bar on phasing computed at the NR merger. Here and below the instant of "merger" is defined as the time of the location of the peak of the modulus of the $\ell = m = 2$ waveform. This error bar was estimated by computing the value at (the highest-resolution) merger of the phase difference between the highest (H) and second-highest (SH) resolutions available in the catalog, $\delta^{\rm NR}\phi(t) \equiv \phi^{\rm H}(t) - \phi^{\rm SH}(t)$. This difference is monotonically varying[1] up to merger and, by definition, taken to be zero at the start of the two simulations. When only one resolution is available we do not indicate any phasing uncertainty in Table I. In such cases one can check the consistency by looking at data sets with neighboring parameters. In SXS simulations, the data are extracted at finite radius and then extrapolated to future null infinity (e.g. [27,28]). This is done by means of a fit using a polynomial in $1/r$, where r is the extraction radius. The user of the catalog is free to choose between different orders of extrapolation ($N = 2$, 3, 4) depending on the application, with the warning that the "best" extrapolation order to use depends on the simulation and that higher extrapolation orders tend to do better during the inspiral and worse during ringdown. We found experimentally that extrapolation order $N = 3$ is reliable for all data sets except for SXS:BBH:0002, where we used $N = 2$ to reduce unphysical oscillations during the late inspiral. In addition to the data of the catalog, we also use a ∼14 orbits $q = 1$, $\chi = 0$ waveform [19], that was used to calibrate earlier EOB models [9,29].

[1] $\delta^{\rm NR}\phi(t)$ is monotonically *increasing* with t except for the data sets SXS:BBH:0178 and SXS:BBH:0065 where it is monotonically *decreasing*.

B. Data from the Llama code

We use a sample of 10 configurations simulated with the Llama code, five of them being computed with two different resolutions. All but one of them have mass ratio $q = 1$. The dimensionless spin values that we consider are $\chi = (\pm 0.8, \pm 0.6, \pm 0.4, \pm 0.2, 0)$. The precise configurations (and resolutions used) are listed in Table II. The two nonspinning configurations were first presented in Ref. [26]; the remaining, equal-mass, spinning configurations were first presented in Ref. [30]. They were here simulated at higher resolutions and with improved grid setups to enhance accuracy. For all Llama data the waveforms at future null infinity are estimated by using Cauchy-characteristic extraction (CCE) [31,32].

The Llama simulations are relatively short (between 4 and 8 orbits). We use them mainly for reaching one of the main aims of this paper, namely to check to what extent the EOB prediction for the *energetics* of the system [as measured by the gauge-invariant relation $E_b(j)$ between the dimensionless binding energy and the angular momentum] is consistent with the corresponding NR quantity.

The longer SXS waveforms (between 12 and 32 orbits) not only were used to check the phasing performance of the EOB model, but also its energetics (modulo subtleties related to junk radiation discussed below, which are essentially absent when dealing with Llama data). The joined use of Llama and SXS waveform data allowed us to (i) reach a reliable NR calibration of the spinning EOB model of Paper I; (ii) perform interesting cross checks on

energy and angular momentum *at merger* between NR data obtained with completely different codes; and (iii) compute the $E_b(j)$ energetics for a large sample of spin-aligned SXS data [thereby improving on Ref. [11] where only two $E_b(j)$ curves were computed].

III. IMPROVED CALIBRATION OF THE NONSPINNING EOB MODEL

As mentioned in the Introduction, the spinning EOB model considered in this paper is essentially the one introduced in Paper I (to which we refer for our notation), in particular the waveform up to merger is defined by Eqs. (75)–(96) there. The only change in the theoretical framework concerns the definition of the EOB radial potential A. In the present work, we use the full 4PN-accurate analytical knowledge of the EOB radial interaction (see below). In addition we *extended* (without any additional theoretical modification) the application of the new ringdown description of Ref. [14] to the full SXS data sets of Table I. For the equal-mass, equal-spin configurations, the ringdown description is exactly as described in Ref. [14], including the use of the fitting coefficients listed in Table II there. On the other hand, for the remaining configurations in our Table I we do not make use of the latter fit, but rather we apply the ringdown modelization methodology of [14] separately to each data set. We postpone to future work the construction of a global analytical extrapolation of the latter, discrete, ringdown data.

We use here the 5PNlog-accurate post-Newtonian expansion of the orbital $A^{\rm PN}_{\rm orb}$ function

$$A^{\rm PN}_{\rm orb}(u_c) = 1 - 2u_c + 2\nu u_c^3 + \nu a_4 u_c^4 + \nu[a_5^c(\nu) + a_5^{\log}\ln u_c]u_c^5 + \nu[a_6^c(\nu) + a_6^{\log}\ln u_c]u_c^6, \quad (1)$$

where

$$\nu \equiv \frac{\mu}{M} = \frac{m_1 m_2}{(m_1+m_2)^2} = \frac{q}{(1+q)^2} \quad (2)$$

is the main deformation parameter of EOB theory, which varies between $\nu = 0$, in the large-mass-ratio limit ($q = m_1/m_2 \gg 1$) and $\nu = 1/4$ in the equal-mass case. The dimensionless gravitational potential u_c is defined as $u_c = M/r_c$ in terms of the EOB centrifugal radius

$$r_c \equiv \sqrt{r^2 + a^2 + \frac{2Ma^2}{r} + \delta a^2(r)}. \quad (3)$$

Here the (next-to-leading-order) correction of the Kerr parameter, $\delta a^2(r)$ [12], is defined in Eq. (59) of Paper I. Contrary to Paper I, where we had phenomenologically fixed the 4PN coefficient $a_5^c(\nu)$ to the (ν-independent) fiducial value $a_5^c = 23.5$, we use here the exact, ν-dependent, analytical expression of $a_5^c(\nu)$ obtained in Ref. [33] (see also [34]). We recall that the orbital EOB radial potential $A_{\rm orb}$ is defined by Padé resumming $A^{\rm PN}_{\rm orb}(u_c)$ as

$$A_{\rm orb}(u_c;\nu;a_6^c) = P^1_5[A^{\rm PN}_{\rm orb}(u_c)]. \quad (4)$$

In view of the change in the analytical expression of $A_{\rm orb}$, our first task will be to provide a new calibration of the single, effective 5PN functional parameter $a_6^c(\nu)$ entering $A_{\rm orb}$. We perform this calibration by means of a sample of *nonspinning* waveforms. (This nonspinning-calibrated orbital potential will then be used as is in our spinning EOB model.) We use as calibrating waveforms eight SXS simulations with mass ratio $q = (1, 1.5, 2, 3, 4, 5, 6, 8)$ (the $q = 9.989$ one is used just as a cross-check). For $q = 1$ we use the same $\sim$14 orbits waveform that was used in the calibration procedure of Ref. [29]. We tune $a_6(\nu)$ so that the EOB and NR phasing agree (after a suitable alignment) within the NR phasing error at NR merger. Following the footsteps of Ref. [29] (and in particular the cross-check of the time-domain analysis with the Q_ω analysis) we obtained

$$a_6^c(\nu) = 3097.3\nu^2 - 1330.6\nu + 81.38. \quad (5)$$

Note that $a_6^c(\nu)$ varies between -57.69 for $\nu = 0.25$ (equal-mass case) and -7.432 for $q = 9.989$ ($\nu \approx 0.0827$). Moreover the parameter $\Delta t_{\rm NQC}$, given the time lag between the peak of the pure orbital frequency $\Omega_{\rm orb}$ [see Eq. (100) of Paper I] and the EOB/NR matching point on the time axis (which is used to determine next-to-quasicircular (NQC) corrections to the waveform) is fixed (as discussed in Sec. V of Paper I) as $\Delta t_{\rm NQC}(\chi = 0) = 1M$ in the nonspinning case.[2] Finally, as mentioned in the Introduction, we use the new modelization of the ringdown introduced in Ref. [14]. In this paper, we use the actual fitting coefficients as obtained applying the procedure of Ref. [14] to each single waveform. The performance of suitable "fits of fits" extending the validity of the procedure of Ref. [14] outside the domain of known waveforms will be discussed elsewhere.

Figure 1 (which plots the Regge-Wheeler-Zerilli normalized waveform $\Psi_{22} \equiv Rh_{22}/\sqrt{24}$) illustrates the EOB/NR phase agreement, for $q = 1$ when using (i) the 14-orbit (up to merger) calibration waveform (top panel); (ii) the $\sim$28-orbit SXS:BBH:0066 waveform of the catalog; and (iii) the longest NR waveform available in the catalog, SXS:BBH:0002, that corresponds to about 32 orbits up to merger. We stress that the actual calibration of $a_6^c(\nu)$ made use neither of SXS:BBH:0066 nor of SXS:BBH:0002, which are used here just to provide an independent check of the calibration procedure. The vertical lines in the plots highlight the alignment time intervals, corresponding to dimensionless GW frequencies $(M\omega_L, M\omega_R)$. To check

[2]By contrast, in the case of high, positive spins, $\chi \geq 0.85$, it is useful to allow $\Delta t_{\rm NQC}$ to depend on the spin (see below).

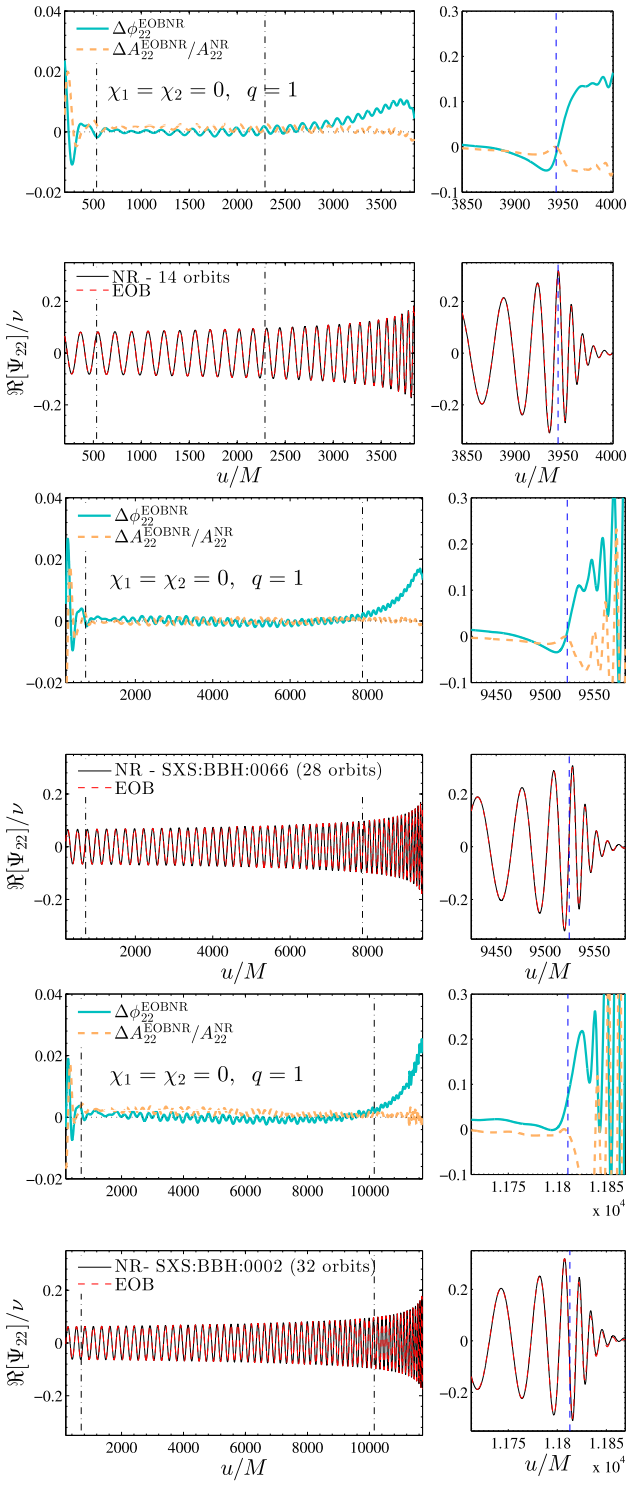

FIG. 1. EOB/NR $\ell = m = 2$ waveform comparison: $q = 1$, $\chi_1 = \chi_2 = 0$ and $a_6^c(0.25) \approx -57.688$ from Eq. (5). The calibration was done using the 14-orbit simulation, following the same procedure as in Ref. [29] (that was also using the same data set). The resulting EOB waveform is then checked for consistency against waveforms SXS:BBH:0066 (∼28 orbits, middle panel) and SXS:BBH:0002 (∼32 orbits, bottom panel), that is the longest NR waveform currently available. The EOB/NR modulus and phase agreement is excellent all through inspiral, plunge, merger and ringdown.

consistency, we fixed $M\omega_R = 0.045$ for each data set. Then, we use $M\omega_L = 0.035$ for the 14-orbit run, $M\omega_L = 0.023$ for SXS:BBH:0066 and $M\omega_L = 0.025$ for SXS:BBH:0002. In the latter case, the phase difference between EOB and NR, accumulated up to NR merger, $\Delta\phi_{\rm mrg}^{\rm EOBNR} \equiv \phi_{\rm mrg}^{\rm EOB} - \phi_{\rm mrg}^{\rm NR} = 0.073$ rad is comparable to the NR uncertainty at merger, ≈0.066 rad (see Table I). Similarly, when using $a_6^c(\nu)$ as given by Eq. (5), one finds that the EOB/NR phase difference is comparable to (though in some cases slightly larger than) the NR uncertainty at merger for all nine nonspinning data (compare columns seven and eight in Table I).

IV. ENERGETICS OF NONSPINNING COALESCENCES: THE CHOICE $\mathcal{F}_{r_*} = 0$

A. Energetics with (nonspinning) Llama data

Having used SXS phasing data to determine the relation Eq. (5), let us now turn to discussing the energetics of the model, motivating, in particular, the choice of a vanishing radial component of radiation reaction that we made here. The choice $\mathcal{F}_{r_*} = 0$, was introduced in Ref. [35] and used in several previous EOB works [26,36,37]) as well as in Paper I. As in previous works [26,37,38], the analysis of the energetics is done via the gauge-invariant relation between the dimensionless binding energy E_b and the dimensionless total angular momentum, j, $E_b(j)$. These quantities are computed as

$$E_b \equiv \frac{M^0_{\rm ADM} - \Delta\mathcal{E}_{\rm rad} - M}{\mu}, \tag{6}$$

$$j \equiv \frac{\mathcal{J}^0_{\rm ADM} - \Delta\mathcal{J}_{\rm rad}}{M\mu}. \tag{7}$$

Here $(M^0_{\rm ADM}, \mathcal{J}^0_{\rm ADM})$ denote the total, initial Arnowitt-Deser-Misner (ADM) mass energy and angular momentum of the system (including the contribution of the individual spins), $(\Delta\mathcal{E}_{\rm rad}, \Delta\mathcal{J}_{\rm rad})$ denote the energy and angular momentum radiated in GWs, while $M = m_1 + m_2$ and $\mu = m_1 m_2/M$, where m_1 and m_2 are the NR measured initial Christodoulou masses. We recall that, while $\Delta\mathcal{E}_{\rm rad}$ is obtained by time-integrating the square of the news ($\dot{h}$), $\Delta\mathcal{J}_{\rm rad}$ is obtained by time-integrating a bilinear expression in the news and the strain h. To obtain the strain we start from the Fourier transform of ψ_4 and use the method of [39]. The $E_b(j)$ relation can be straightforwardly obtained from the results of the BBH simulations obtained with the Llama code [40,41], as we did in a previous study [26] limited to nonspinning BBHs. On the other hand, when using SXS data, several subtleties have to be properly addressed in order to accurately estimate the $E_b(j)$ relation (see the Appendix for details).

Figure 2 displays the $E_b(j)$ relation in the $q = 1$, nonspinning case. It shows the triple comparison between

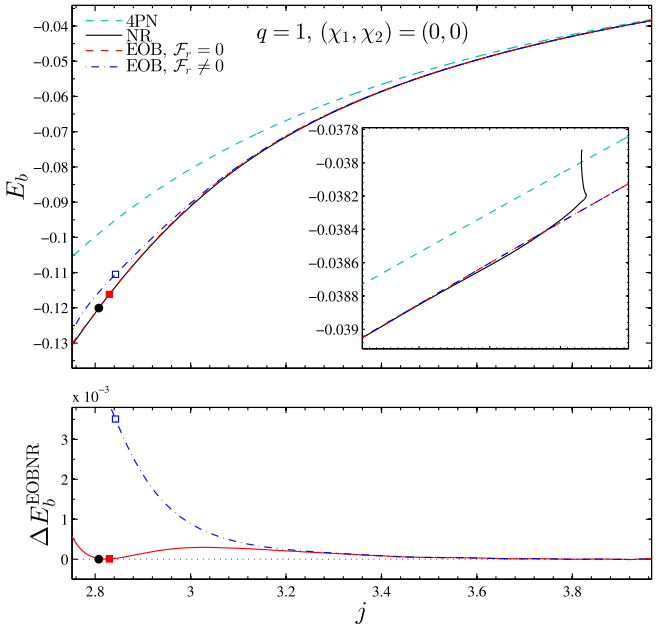

FIG. 2. Energetics for $q = 1$, nonspinning binary: comparison between NR Llama data, the 4PN, Taylor-expanded, curve and two EOB curves, one with and the other without a radial part of the radiation reaction $\mathcal{F}_{r_*}$. The (effective) choice $\mathcal{F}_{r_*} = 0$ displays the smallest ($\sim 10^{-4}$) discrepancy with NR data up to merger (indicated by colored markers). The inset focuses on the initial transient driven by junk radiation.

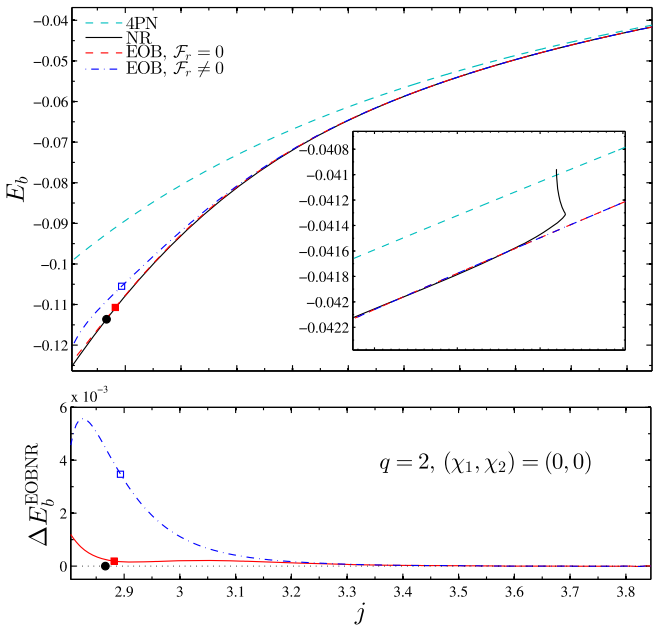

FIG. 3. Energetics comparison, as in Fig. 2, but for $q = 2$, nonspinning, Llama NR data. The $\mathcal{F}_{r_*} = 0$ curve displays the smallest discrepancy with NR data up to merger (indicated by colored markers).

the NR curve and (i) the PN-expanded $E_b(j)$ relation; (ii) the EOB model with a_6^c given by Eq. (5) and with the choice $\mathcal{F}_{r_*} = 0$; (iii) exactly the same EOB model [in particular, with the value of a_6^c given by Eq. (5)] but with the (nonresummed), 2.5PN accurate, expression of $\mathcal{F}_{r_*}$ of Ref. [42]. Note that the latter expression was already used in previous EOB work [29], though its effect on $E_b(j)$ is investigated here for the first time.

The general structure of the PN-expanded $E_b(j;\chi_1,\chi_2)$ relation is (in the spinning case)

$$E_b^{\rm PN} = \sum_{n=2}^{10} \frac{c_n(\nu;\chi)}{\ell^n}, \tag{8}$$

where $\ell = j - (\frac{m_1}{m_2}\chi_1 + \frac{m_2}{m_1}\chi_2)$ denotes the dimensionless *orbital* angular momentum, $\ell = L/(\mu M)$ and the coefficients $c_n(\nu;\chi)$ depend at most quadratically on the dimensionless spins $\chi_1 \equiv S_1/m_1^2$, $\chi_2 \equiv S_2/m_2^2$. The accuracy we use in $E_b^{\rm PN}$ is 4PN in the nonspinning sector [43]; NNLO for the spin-orbit and NLO for the spin-spin part (see e.g. [44]).

As shown in Fig. 2 [see especially the bottom panel, which displays $\Delta E_b^{\rm EOBNR}(j) \equiv E_b^{\rm EOB}(j) - E_b^{\rm NR}(j)$] the use of a vanishing radial radiation reaction leads, from an effective point of view, to a better agreement between the EOB energetics and the NR one up to merger.[3] The NR and EOB merger points are indicated, respectively, by a filled circle (NR), by a filled square (EOB, $\mathcal{F}_{r_*} = 0$) and by an empty square (EOB, $\mathcal{F}_{r_*} \neq 0$). By contrast, the PN curve shows the largest deviation from NR results, especially at low j's. Finally, Fig. 3 shows that the same conclusions hold true also for the $q = 2$ Llama data.

As discussed in Refs. [35,45], there exists a coordinate gauge where $\mathcal{F}_{r_*} = 0$. Further work [42] has shown that the requirement of the vanishing of the Schott contribution $J^{\rm Schott}$ to the angular momentum required a specific, nonzero value of $\mathcal{F}_{r_*}$ (which was then used in Ref. [29] because the vanishing of $J^{\rm Schott}$ seemed *a priori* required by the definition of the azimuthal component $\mathcal{F}_\varphi$ of the radiation reaction within the EOB formalism). However, because of the various approximations made in defining $\mathcal{F}_\varphi$ in the EOB formalism, it is not actually required to choose the $\mathcal{F}_{r_*}$ that is implied by a vanishing $J^{\rm Schott}$. Our present work experimentally shows that the condition $\mathcal{F}_{r_*} = 0$ is a simple and effective way to accomplish a (rather surprisingly) good agreement between the numerical and EOB $E_b(j)$ curves. We leave to future work a theoretical study of why such a condition, in conjunction with the current approximate value of $\mathcal{F}_\varphi^{\rm EOB}$, happens to lead to rather small values of both $J^{\rm Schott}$ and $E_b^{\rm Schott}$ (as shown in Figs. 2–3 above).

[3]We found that a different calibration of a_6^c is unable to displace the $\mathcal{F}_{r_*} \neq 0$ curve on top of the NR one.

TABLE III. The shift vector $(\Delta j^0, \Delta E_b^0)$ that is applied to the raw $E_b(j)$ curves computed for an illustrative subset of the configuration listed in Table I. The numbers listed refer to curves where the final state (j_f, M_f) was already imposed on the raw data, except for those data sets marked with an asterisk, *.

Name	q	χ_1	χ_2	ΔE_b^0	Δj^0
SXS:BBH:0066	1	0	0	−5.583e-03	−2.13e-02
SXS:BBH:0169	2	0	0	+1.224e-05	−5.0e-04
SXS:BBH:0030	3	0	0	−1.669-03	−9.0-03
SXS:BBH:0167	4	0	0	+1.917e-04	+7.0e-04
SXS:BBH:0056	5	0	0	−2.571-03	−1.25-02
SXS:BBH:0166	6	0	0	+1.942e-04	+7.0e-04
SXS:BBH:0063	8	0	0	−7.7709e-04	−4.0-03
SXS:BBH:0185	9.989	0	0	+4.053e-04	−2.4-03
SXS:BBH:0156	1	−0.95	−0.95	−9.496e-05	−6.0-03
SXS:BBH:0154 *	1	−0.80	−0.80	−3.018e-04	−0.9-03
SXS:BBH:0151 *	1	−0.60	−0.60	−6.507e-05	−5.7e-04
SXS:BBH:0149	1	−0.20	−0.20	−4.460e-04	−3.8-03
SXS:BBH:0150	1	+0.20	+0.20	−4.200e-04	−2.8-03
SXS:BBH:0152 *	1	+0.60	+0.60	−7.393e-05	−0.7-03
SXS:BBH:0155 *	1	+0.80	+0.80	−2.536e-04	−0.5-03
SXS:BBH:0172	1	+0.98	+0.98	−3.640-03	−1.05-02
SXS:BBH:0178	1	+0.994	+0.994	−2.657-03	−8.8-03
SXS:BBH:0162	2	+0.60	0	−5.240e-04	−2.3-03
SXS:BBH:0036	3	−0.50	0	−2.434-03	−5.5-03
SXS:BBH:0031	3	+0.50	0	−2.326-03	−7.1-03
SXS:BBH:0064	8	−0.50	0	−4.604-03	−5.5-03
SXS:BBH:0065	8	+0.50	0	−4.792-03	−6.8-03

B. Energetics with (nonspinning) SXS data

We found that a similar excellent agreement among energetics holds, up to merger for all nonspinning SXS configurations at our disposal, which cover the mass-ratio range $1 \leq q \leq 9.989$. (For a previous comparison of nonspinning merger characteristics see Ref. [46]).

So far, the only published computation of the energetics from SXS data was presented in Ref. [11]. It was limited to two, quasiextremal, spinning configurations with spin either aligned or antialigned with the orbital angular momentum, with $\chi_1 = \chi_2 = -0.95$ and $\chi_1 = \chi_2 = +0.98$.

We present here the first systematic computation of $E_b(j)$ curves from SXS data covering a large sample of nonprecessing, spinning (and nonspinning) configurations. We computed $E_b(j)$ curves from the nonspinning binaries in Table I applying the same standard procedure we used for Llama data. Note, however, that, while the time integration of energy and angular momentum losses from Llama data could be meaningfully performed starting at the beginning of the simulation, in the case of SXS data, we found it necessary to correct the time integration of the early "junk-radiation" losses by adding a vectorial shift $(\Delta j^0, \Delta E_b^0)$ in the (j, E_b) plane. This shift was essentially determined so as to minimize the EOB/NR difference $\Delta E_b^{\rm EOBNR}(j)$ during the early inspiral. All technical details of our computation are explained in the Appendix [see in particular Table III, that lists the values of the vectorial shifts $(\Delta j^0, \Delta E_b^0)$ we used].

The main results of our SXS-data analysis are (i) for $q = 1$ and $q = 2$, the energetics computed from SXS data confirms the results based on Llama data given above in Figs. 2–3; (ii) for the other values of q, $3 \leq q \leq 9.989$, not covered by Llama data, we again find an excellent consistency between the energetics of our EOB model and the SXS NR one; (iii) it is in particular remarkable that the binding energy and angular momentum *at merger* $(E_b^{\rm mrg}, j_b^{\rm mrg})$ provided by our EOB model are in accurate agreement with the NR one.[4] These results are exemplified in Figs. 4, 5 and 6.

For illustrative purposes, Fig. 4 explicitly shows the $q = 8$ case, data set SXS:BBH:0063. The bottom panel shows the EOB-NR difference. The vectorial shift in the (j, E_b) plane used here is $\Delta j^0 = -4 \times 10^{-3}$, $\Delta E_b^0 = -7.7709 \times 10^{-4}$ [so that $E_b(j) \equiv E_b^{\rm raw}(j - \Delta j^0) + \Delta E_b^0$]. As discussed in detail in the Appendix these (quite small) shifts are determined through the following two-step procedure. Step 1: Δj^0 is determined first, by requiring that the difference between the EOB and NR dimensionless orbital

[4] As mentioned above, we recall that the instant of the merger is defined, both in EOB and NR, as the time when the modulus of the $\ell = m = 2$ waveform reaches its maximum.

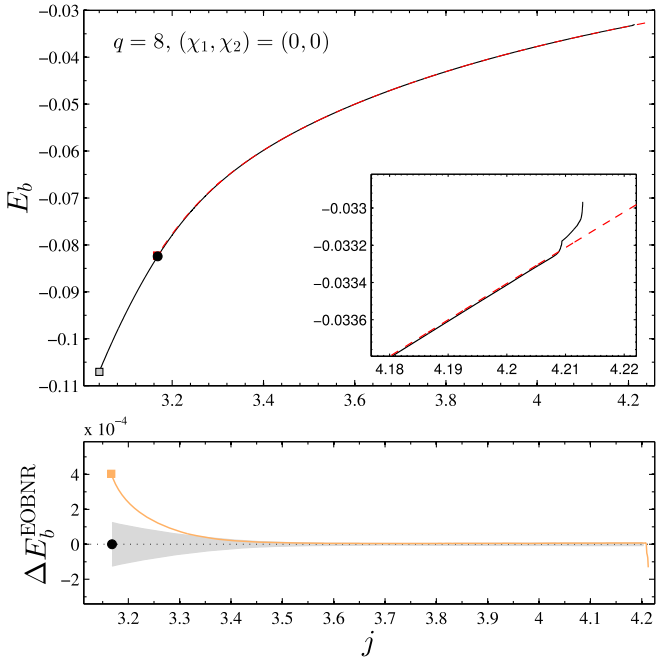

FIG. 4. Comparison between EOB and SXS energetics for the $q = 8$ case. The shaded area indicates numerical uncertainty measured taking the difference between the highest and second highest resolution data. Note that the EOB merger state (red, filled square marker) and the NR merger state (black filled, circle) are barely distinguishable in the upper panel.

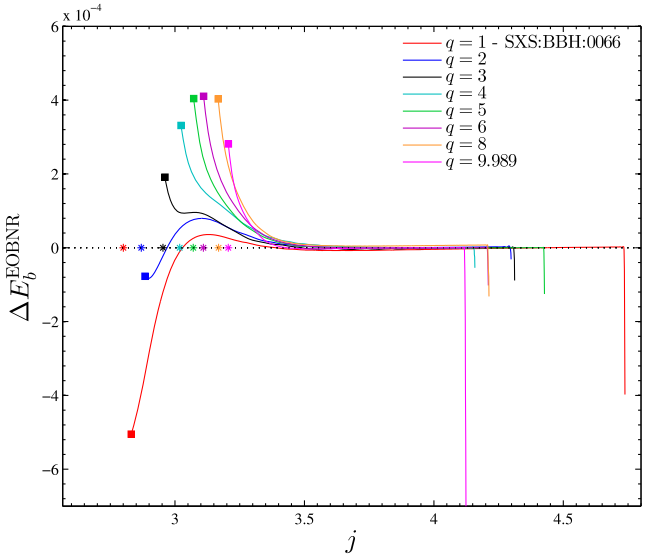

FIG. 5. EOB/NR differences between $E_b(j)$ curves for all but one ($q = 1.5$) nonspinning SXS data of Table I. The difference is compatible with NR uncertainties up to merger ($\sim 10^{-4}$; see Fig. 4 for the illustrative $q = 8$ case).

frequencies (defined as $\hat{\Omega} = \partial E_b/\partial j$) $\Delta\hat{\Omega}^{\rm EOBNR}(j) = \hat{\Omega}^{\rm EOB}(j) - \hat{\Omega}^{\rm NR}(j)$ oscillates around zero on the largest possible j interval. With a so-chosen Δj_0, one finds that $\Delta\hat{\Omega}^{\rm EOBNR}$ oscillates between $\pm 5 \times 10^{-5}$ over the interval $3.6 \lesssim j \lesssim 4.2$. Step 2: the constant ΔE_b^0 is then determined by minimizing the difference $\Delta E_b^{\rm EOBNR}(j) \equiv E_b^{\rm EOB}(j) - E_b^{\rm raw}(j - \Delta j^0)$, which is essentially constant on a large j interval, during the early inspiral. After adding these small shifts to the raw data, one finds that $\Delta E_b^{\rm EOBNR}(j)$ is of the order of $\pm 10^{-5}$ for $3.5 \lesssim j \lesssim 4.2$.

The shaded area in the bottom panel of Fig. 4 indicates the numerical uncertainty, as estimated by taking the difference between the (raw) $E_b(j)$ curves obtained from the highest (Lev5) and second-highest (Lev4) resolution data present in the SXS catalog. In order to get a conservative uncertainty estimate, we do not apply any vectorial shift to the raw data. Let us emphasize the remarkable agreement between EOB and NR energetics *at merger*. The difference at the NR merger point is of order 4×10^{-4}, which is barely visible in the top panel of Fig. 4 (and it is approximately twice the estimated uncertainty there).

For the other nonspinning configurations in Table I, one obtains curves quite analogous to the $q = 8$ case. The relevant information is displayed in Fig. 5 that collects the $\Delta E_b^{\rm EOBNR}(j) \equiv E_b^{\rm EOB}(j) - E_b^{\rm NR}(j)$ differences for all nonspinning data but one (the $q = 1.5$ one). Note that the end points indicated by square markers in Fig. 5, record the values of the function $\Delta E_b^{\rm EOBNR}(j)$ at the corresponding EOB merger values of j, $j_{\rm mrg}^{\rm EOB}$. On the other hand, the stars on the x-axis of the figure mark the corresponding NR merger values of j, $j_{\rm mrg}^{\rm NR}$.

For $q = 1$, we use here the SXS:BBH:0066 data set with ~ 28 orbits. The vectorial shifts $(\Delta j_b^0, \Delta E_b^0)$ we use are listed in Table III in the Appendix. For all configurations, one finds that the EOB/NR agreement is of the order 10^{-5} at the beginning of the inspiral and grows only up to a few parts in 10^{-4} around merger. These differences are comparable to (though slightly larger than) the corresponding error bars computed, as above, taking the difference between the two highest resolutions available.

In Fig. 6 we complement the above results by focusing on the EOB/NR comparison for merger characteristics, $(j_{\rm mrg}, E_{\rm mrg})$ as a function of ν. The figure shows that the EOB/NR disagreement increases with ν: from a difference of 3.07×10^{-4} for $E_b^{\rm mrg}$ and 1.7×10^{-4} for $j^{\rm mrg}$ for $q = 9.989$ ($\nu = 0.0827$) the EOB model ends up slightly overestimating the NR values in the equal-mass case, $\nu \to 0.25$. In particular, for $\nu = 0.25$ we see that the EOB prediction for $E_b^{\rm mrg}$ is larger than the NR one by 4.9×10^{-3} and that the EOB prediction for $j^{\rm mrg}$ is larger than the NR one by 3.1×10^{-2}. [These differences are larger than those apparent in the corresponding end points of Fig. 5 because we are now computing $E_b^{\rm EOB}(j_{\rm mrg}^{\rm EOB}) - E_b^{\rm NR}(j_{\rm mrg}^{\rm NR})$ while the vertical displacement of the end points of Fig. 5 corresponded to $E_b^{\rm EOB}(j_{\rm mrg}^{\rm EOB}) - E_b^{\rm NR}(j_{\rm mrg}^{\rm EOB})$]. In the same figure we also display Llama merger data, denoted by

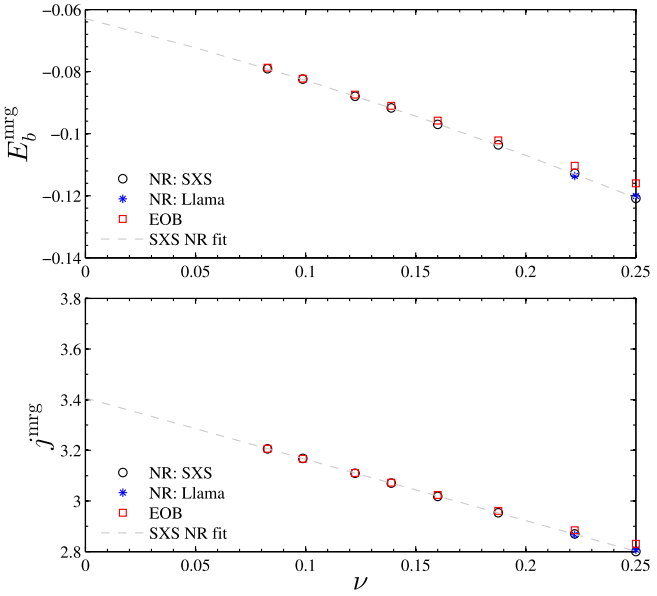

FIG. 6. Binding energy and angular momentum *at merger* (i.e. at the maximum of $|h_{22}|$) for nonspinning binaries versus the symmetric mass ratio ν. The plot shows (i) the highly accurate numerical agreement between SXS and Llama final configurations for $q = 1$ and $q = 2$; (ii) the good numerical consistency between EOB predictions and actual NR states.

asterisks. We find that Llama and SXS data are fully consistent within the 10^{-4} level. Finally, the ν dependence of the SXS NR $E_b^{\rm mrg}$ can be fitted by means of a second order polynomial, while $j^{\rm mrg}(\nu)$ is well fitted by a straight line, namely

$$E_{b,\rm SXS}^{\rm mrg} = -0.062951 - 0.176949\nu - 0.216264\nu^2, \quad (9)$$

$$j_{\rm SXS}^{\rm mrg} = 3.406583 - 2.421052\nu. \quad (10)$$

V. NR CALIBRATION OF THE EOB SPIN-ORBIT COUPLING

Let us now turn to discussing the numerical completion of the EOB spinning model. As mentioned above, the spinning sector of the model we use here is exactly the same as described in Paper I. In the latter work it was shown that it was possible to obtain a good EOB/NR phasing agreement by tuning a *single* effective functional parameter $c_3(\chi)$ that was entering the spin-orbit coupling at next-to-next-to-next leading order.[5] The best values of the parameter c_3, for various spin values, are listed in Table I of Paper I. Since the orbital $A_{\rm orb}$ function has changed, in the present work, because of (i) the use of the complete analytical 4PN information and (ii) the consequently modified functional dependence of $a_c^6(\nu)$ given by Eq. (5), we now need to look for a new determination of $c_3(\chi)$. In doing so, we also consider here more NR simulations than in Paper I, notably taking into account all available nonprecessing data in the SXS catalog. The spinning SXS configurations we use are listed in Table I: the mass ratio varies in the range $1 \le q \le 8$ and there are several configurations where only one of the two black holes is spinning. *A priori*, one expects the NNNLO effective parameter c_3 to be a function of both the mass ratio and the spins of the binary. The determination of c_3 is done in two steps. In a first step, we separately considered each binary configuration and determined a preliminary best value of c_3 by minimizing the EOB/NR phase difference, after alignment in the inspiral phase, so to be compatible with (and typically smaller than) the NR uncertainty. This procedure is rather straightforward, as it is just a one parameter search. In a second step, we looked for a global, analytical representation that approximately reproduces the latter preliminary best values of c_3 as a function of symmetric mass ratio and spins. We found that one can represent, with sufficient accuracy, the values (determined by minimizing the EOB/NR phase difference as explained above) of c_3 for the entire sample of configurations listed in Table I, by means of the following simple functional relation:

$$c_3(\tilde{a}_1, \tilde{a}_2, \nu) = p_0 \frac{1 + n_1(\tilde{a}_1 + \tilde{a}_2) + n_2(\tilde{a}_1 + \tilde{a}_2)^2}{1 + d_1(\tilde{a}_2 + \tilde{a}_2)} + (p_1\nu + p_2\nu^2 + p_2\nu^3)(\tilde{a}_1 + \tilde{a}_2)\sqrt{1 - 4\nu} + p_4(\tilde{a}_1 - \tilde{a}_2)\nu^2, \quad (11)$$

where

$$p_0 = 44.786477, \quad (12)$$

$$n_1 = -1.879350, \quad (13)$$

$$n_2 = 0.894242, \quad (14)$$

$$d_1 = -0.797702, \quad (15)$$

$$p_1 = 1222.36, \quad (16)$$

$$p_2 = -12764.4, \quad (17)$$

$$p_3 = 36689.6, \quad (18)$$

$$p_4 = -358.086, \quad (19)$$

and where we found it convenient to introduce the spin quantities $\tilde{a}_{1,2} \equiv X_{1,2}\chi_{1,2}$, with $X_{1,2} \equiv m_{1,2}/M$, and $M = m_1 + m_2$. With our convention that $m_1 > m_2$, in terms of the symmetric mass ratio ν we have

[5]The analysis of Paper I was limited to the equal-mass, equal-spin case.

$$X_1 = \frac{1}{2}(1+\sqrt{1-4\nu}), \tag{20}$$

and $X_2 = 1 - X_1$. The terms in Eq. (11) that vanish in the equal-mass, equal-spin case were chosen, for simplicity, to be linear in the spins. Similarly, the polynomial dependence in ν was found necessary to properly fit the values of c_3 yielding a good NR/EOB phasing agreement for $q = 8$, $(\chi_1, \chi_2) = (+0.5, 0)$, SXS:BBH:0065 configuration. In the equal-mass, equal-spin (aligned, or antialigned with the orbital angular momentum) case, one finds that the dependence of c_3 on the spin is nearly linear (see Fig. 7).

Finally, let us mention that, as already discussed in Paper I (see Table I there) we found it necessary to flex the simple choice $\Delta t_{\rm NQC} = 1M$, uniformly used in the nonspinning case, so as to allow it to depend on spin for large, positive, spins. Actually, the only available simulations where we found the need of flexing $\Delta t_{\rm NQC}$ are the six equal-mass, equal-spin configurations with $\chi = \chi_1 = \chi_2 > \chi_0 = +0.85$. In practice, for spins $\chi = \{+0.90, +0.95, +0.97, +0.98, +0.99, +0.994\}$ we found as good choices $\Delta t_{\rm NQC} = \{0.2, -1.2, -1.7, -2.0, -3.0, -3.2\}$, respectively. In the EOB numerical evolution we use a time-resolution $\Delta t^{\rm EOB} = 0.1M$, and $\Delta t_{\rm NQC}$ is chosen as an integer multiple of $\Delta t^{\rm EOB}$. The values of $\Delta t_{\rm NQC}$ listed above are accurately fitted by using a (1,1) Padé approximant:

$$\Delta t_{\rm NQC}(\chi) = \frac{1 + n_1(\chi - \chi_0)}{1 + d_1(\chi - \chi_0)} \tag{21}$$

with $n_1 = -16.06288$ and $d_1 = -4.04266$ and $\chi_0 = 0.85$.

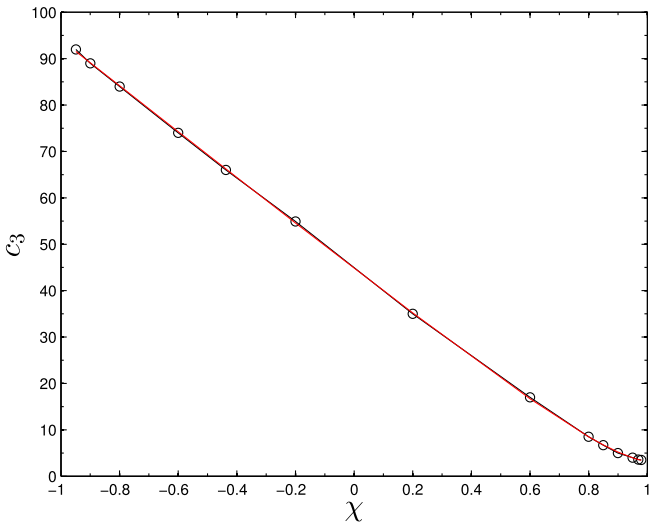

FIG. 7. Quasilinear behavior of the NNNLO effective spin-orbit coefficient $c_3(\hat{a}_1, \hat{a}_2, \nu)$, Equation (11), in the equal-mass ($\nu = 0.25$), equal-spin $\hat{a}_1 = \hat{a}_2 = \chi$ case. The tuning of this single dynamical parameter allows one to get an excellent EOB/NR phasing agreement throughout inspiral, plunge, merger and ringdown.

The quality of the fit yielded by Eq. (11) (together with the discrete values of $\Delta t_{\rm NQC}$ listed above) is quantitatively assessed by measuring the EOB-NR phase difference at NR merger after having aligned (in time and phase) the EOB waveforms to the NR waveform during the early inspiral. Such differences are listed as $\Delta\phi^{\rm EOBNR}_{\rm mrg}$ in Table I. The same table also clearly illustrates the compatibility of the EOB model with the numerical phase uncertainties $\delta\phi^{\rm NR}_{\rm mrg}$ at merger all over the waveform sample considered. The use, in addition to Eq. (11), of the fit (21) slightly worsens $\Delta\phi^{\rm EOBNR}_{\rm mrg}$ as indicated by the values in parentheses in Table I. Anyway, both values are approximately within (half of) the numerical error bar.

Let us emphasize that the EOB/NR agreement remains excellent for the near-extremal spinning cases $\chi_1 = \chi_2 = +0.98$ and $\chi_1 = \chi_2 = +0.994$. Figure 8 shows the EOB/NR comparison obtained by performing the usual time-domain comparison when aligning the waveforms on the frequency interval $(M\omega_L, M\omega_R)$ corresponding to the time-interval indicated by the two vertical dashed lines in the plot. Analogous (or better) plots are found for all other configurations. As an indicator of this good EOB/NR agreement we just give in Table I the values of the phase difference at merger.

To further demonstrate the high quality of the EOB model presented here, and to give a clearer physical meaning to the phase differences quoted above, we also measured the agreement between the EOB waveforms and all the available NR ones by computing the EOB/NR unfaithfulness (as a function of the total mass M)

$$\bar{F}(M) \equiv 1 - \max_{t_0,\phi_0} \frac{\langle h^{\rm EOB}_{22}, h^{\rm NR}_{22}\rangle}{\|h^{\rm EOB}_{22}\|\|h^{\rm NR}_{22}\|}, \tag{22}$$

where t_0 and ϕ_0 are the initial time and phase, $\|h\| \equiv \sqrt{\langle h, h\rangle}$, and the inner product between two waveforms is defined as $\langle h_1, h_2\rangle \equiv 4\Re \int_{f^{\rm NR}_{\rm min}(M)}^{\infty} \tilde{h}_1(f)\tilde{h}_2^*(f)/S_n(f)df$, where $S_n(f)$ is the zero-detuned, high-power noise spectral density of advanced LIGO [47] and $f^{\rm NR}_{\rm min}(M) = \hat{f}^{\rm NR}_{\rm min}/M$ is the *starting frequency of the NR waveform* (after the junk radiation initial transient). Both EOB and NR waveforms are tapered in the time domain so as to reduce high-frequency oscillations in the corresponding Fourier transforms. The procedure of tapering the waveforms is the same followed by Ref. [11], that introduced a different EOB model calibrated to NR, called SEOBNRv2, and performed the same unfaithfulness analysis we are doing here. Figure 9 shows the so-computed unfaithfulness as a function of the total mass of the binary for all configurations we considered. The maximum of $\bar{F}(M)$ is also listed, for convenience, in the last column of Table I. One sees that for most of all considered configurations the value of $\bar{F}$ always stays one order of magnitude below the reference value of 1% (actually, most configurations range between

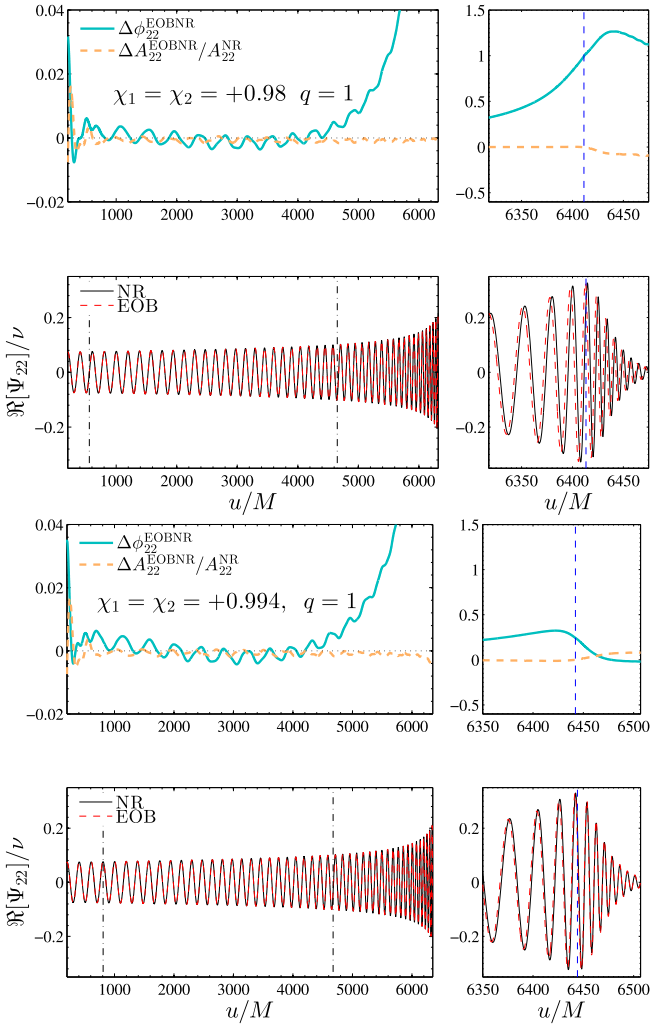

FIG. 8. Illustrative EOBNR time-domain phasing comparison for quasiextremally spinning binaries: $(q,\chi_1,\chi_2) = (1,+0.98,+0.98)$, data set SXS:BBH:0172 (top panel), and $(q,\chi_1,\chi_2) = (1,+0.994,+0.994)$, data set SXS:BBH:0178 (bottom panel). In both cases, the EOBNR difference at merger (dashed vertical line) is within the corresponding NR uncertainty, that is ∼2 rad for $\chi = +0.98$ and ∼0.53 rad for $\chi = +0.994$ (see Table I).

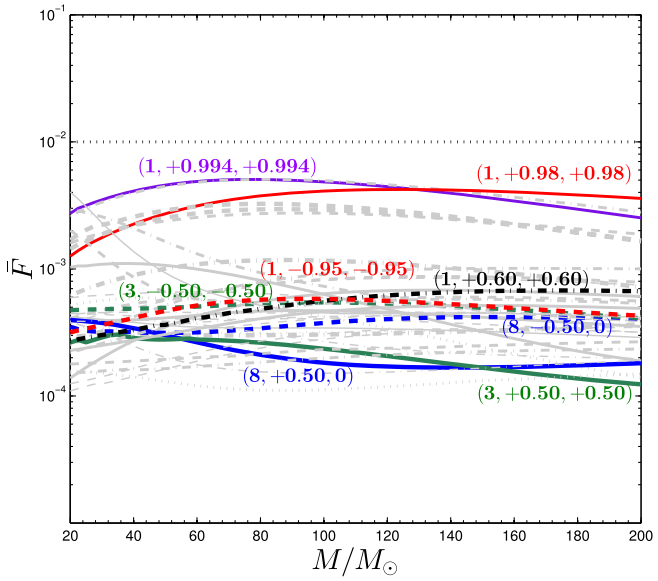

FIG. 9. Unfaithfulness of the $\ell = m = 2$ EOB waveforms with respect to the NR ones for all BBH data sets of Table I. The largest values of $\bar{F}$ corresponds to the quasiextremal spinning configurations SXS:BBH:0177 and SXS:BBH:0178 in Table I. The labels of the configurations use the notation (q,χ_1,χ_2); they are highlighted in color so as to ease a direct comparison with Fig. 1 of Ref. [11].

0.1% and 0.01%) as the total mass of the binary ranges from 20 to $200M_\odot$. Such a waveform quality implies a negligible loss in event rate due to the modeling uncertainty within the frequency range $f \geq f_{\rm min}^{\rm NR}(M)$. Note, however, that the NR waveforms do not cover the entire frequency band of the detector when $M \lesssim 100M_\odot$. For example, the longest NR waveform available, SXS:BBH:0002, has $f_{\rm min}^{\rm NR}(M) \approx 900(M_\odot/M)$ Hz, so that it starts at a frequency ≤ 10 Hz when $M \geq 90M_\odot$ (and ≤ 20 Hz when $M \geq 45M_\odot$). The corresponding value of the unfaithfulness for $M = 90M_\odot$ is $\bar{F} = 8.54 \times 10^{-4}$. For the highest spinning waveform, SXS:BBH:0178, we have $f_{\rm min}^{\rm NR}(M) \approx 1300(M_\odot/M)$ Hz so that we need $M \geq 130M_\odot$ to reach $f_{\rm min}^{\rm NR} = 10$ Hz. However, several recent works have shown that the EOB formalism provided the best available description of GW phasing even during early inspiral [48–50]. In absence of longer NR waveforms able to cover the entire frequency range of the detector for $M \geq 20M_\odot$, the values of $\bar{F}(M)$ displayed in Fig. 9 do not have a direct data-analysis meaning over the full plotted mass range $20M_\odot \leq M \leq 200M_\odot$. We, however, expect, notably in view of Ref. [49], that the values of $\bar{F}$ will not significantly degrade when using longer NR waveforms.

Figure 9 highlights in color the same particular configurations that were highlighted in Fig. 1 of Ref. [11], so as to prompt an easy and direct comparison. In addition, Fig. 9 also shows, in purple, the configuration $(+0.994,+0.994)$ that was not available when Ref. [11] was written. Note that the worst global unfaithfulness, of the order of $\max \bar{F} \approx 0.005$, corresponds to the two quasextremal spinning cases $\chi_1 = \chi_2 = (+0.99,+0.994)$; see Table I. A direct comparison with Fig. 1 of Ref. [11] allows us to make the following observations: (i) the configuration $(q,\chi_1,\chi_2) = (1,+0.6,+0.6)$, SXS:BBH:0152, delivers, within our EOB model, $\bar{F}(M) < 10^{-3}$, all over the total mass range considered. The corresponding curve in Fig. 1 of Ref. [11] was starting around $\bar{F} \simeq 4.5 \times 10^{-3}$ for $M = 20M_\odot$, then increasing up to $\bar{F} \simeq 10^{-2}$ for $M \simeq 50M_\odot$ before decreasing again down to 2.5×10^{-3} for $M = 200M_\odot$. Similarly, the other rather extreme case $(q,\chi_1,\chi_2) = (8,+0.5,0.0)$, SXS:BBH:0065, yields here an unfaithfulness of order 4×10^{-4} at $M = 20M_\odot$, that

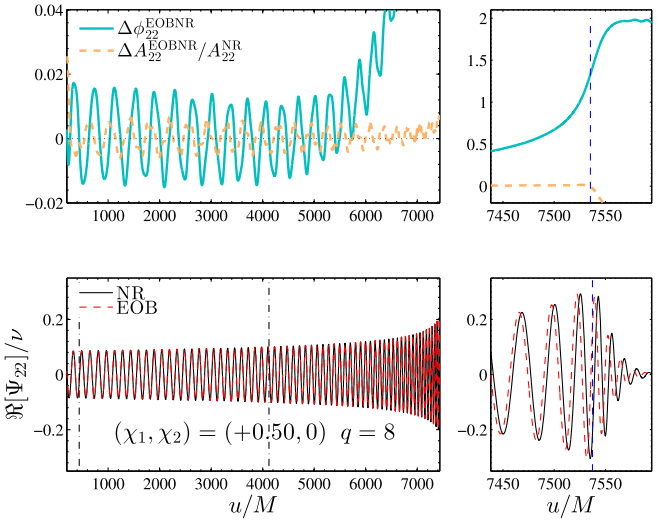

FIG. 10. EOBNR time-domain phasing comparison for SXS: BBH:0065 configuration, $q=8$, $(\chi_1,\chi_2)=(+0.5,0)$. The EOBNR difference at merger (dashed vertical line) is compatible with the corresponding NR uncertainty ~ -3 rad (see Table I). The eccentricity ($\sim 10^{-3}$) modulation in the phase difference is rather visible.

then *decreases* by a factor 2 for larger total mass. By contrast, it is interesting to note that the EOB/NR unfaithfulness computed for the same configuration using SEOBNRv2 *increases* with M from $\approx 0.3\%$ to $\approx 1\%$ (see Fig. 1 of Ref. [11]).

Note that the numerical phase uncertainty on this data set is as large as -3 rad at merger, so that c_3 was (conservatively) calibrated so as to yield a 1.3 rad EOB/NR phase difference at merger (see Fig. 10). We advocate new simulations with reduced error bars for this configuration to firm up (and possibly improve) the current EOB calibration.

Globally, the results collected in Fig. 9 show that our model quantitatively improves upon existing results. We shall discuss more of these and other aspects of our unfaithfulness comparison in the Conclusions (see in particular Fig. 21 and related discussion there).

VI. ENERGETICS FOR SPINNING COALESCENCES

A. Energetics of spinning Llama data

Let us finally discuss the energetics of spinning coalescences yielded by our newly calibrated EOB model. We start doing this with Llama data and we will cross-check our results with SXS data in the next section. Figure 11 contrasts the NR and EOB $E_b(j)$ curves with $\chi_1=\chi_2=(\pm 0.2,\pm 0.4,\pm 0.6)$, with the EOB/NR difference $\Delta E_b(j)$ shown in each bottom subpanel. As before, the EOB (red) and NR (black) mergers are indicated by markers. One sees that the differences are of the order of 10^{-4} (or less) during the inspiral, to grow up to approximately the 10^{-3} level around merger. One also notices that the disagreement between NR and EOB merger quantities depends on the configuration. In several representative cases we have indicated in Fig. 11 an estimate of the NR uncertainty on the energetics. The latter estimate was obtained by first taking the difference between the $E_b(j)$ curves computed from the highest ($\Delta x=0.512$) and second highest ($\Delta x=0.64$) resolution at our disposal and then Richardson extrapolating it assuming some convergence order. The three colored areas around the difference in the bottom panels of Fig. 11 display three different estimates of these NR uncertainties, as obtained by (i) conservatively assuming second order convergence (lighter area); (ii) assuming fourth order convergence; and (iii) assuming eighth order convergence. The most conservative estimate (light grey) may eventually dominate the error budget in the limit of infinite resolution because of the presence of second-order finite difference operators in the numerical infrastructure. This gives bounds of the order $\pm 10^{-3}$ around merger. Such a 10^{-3} level is compatible with the EOB/NR differences at merger that we find for all other configurations. Other sources of uncertainty on the NR data such as (i) the conversion from $\Psi^4_{\ell m}$ to $h_{\ell m}$ [39]; (ii) the CCE error due to the choice of the finite-radius worldtube where the CCE is started [27,51]; or (iii) the effect of higher multipoles, that contribute at the 10^{-4} level are subdominant with respect to the resolution uncertainty.

1. High spins: $\chi_1=\chi_2=\pm 0.8$ (Llama data)

The higher spin values $\chi\equiv\chi_1=\chi_2=\pm 0.8$ deserve a separate discussion. First of all, inspecting the $E_b(j)$ curves one sees that, contrary to the previous cases, the junk radiation transient is such that the "raw" NR curves (depicted as black, dashed lines in Fig. 12) stand visibly below the EOB prediction (for both signs of spin); see insets of the figure. This phenomenon is analogous (though smaller in magnitude) to what we found in nonspinning SpEC data. As mentioned above, it suggests that the NR $E_b(j)$ curve should be corrected by an additional shift vector $(\Delta j^0,\Delta E_b^0)$ so to have consistency with the EOB prediction at large values of j. The phenomenon found here with Llama data is probably due to the fact that the higher multipoles ($\ell\geq 4$) of the junk radiation are not resolved with sufficient accuracy at the spatial resolution we can afford (see below). The error bars, computed as above (though only for one configuration) are also rather large and essentially *constant* over the entire j range. Assuming the conservative second-order convergence order, one sees that the observed energy difference is mostly compatible with the error bar, remaining rather flat up to $j\approx 2$. We then apply the same technique discussed above to determine $(\Delta j^0,\Delta E_b^0)$, i.e., we inspect the EOB/NR differences $\Delta\hat{\Omega}^{\rm EOBNR}(j)$ and $\Delta E_b^{\rm EOBNR}(j)$ and determine the vectorial

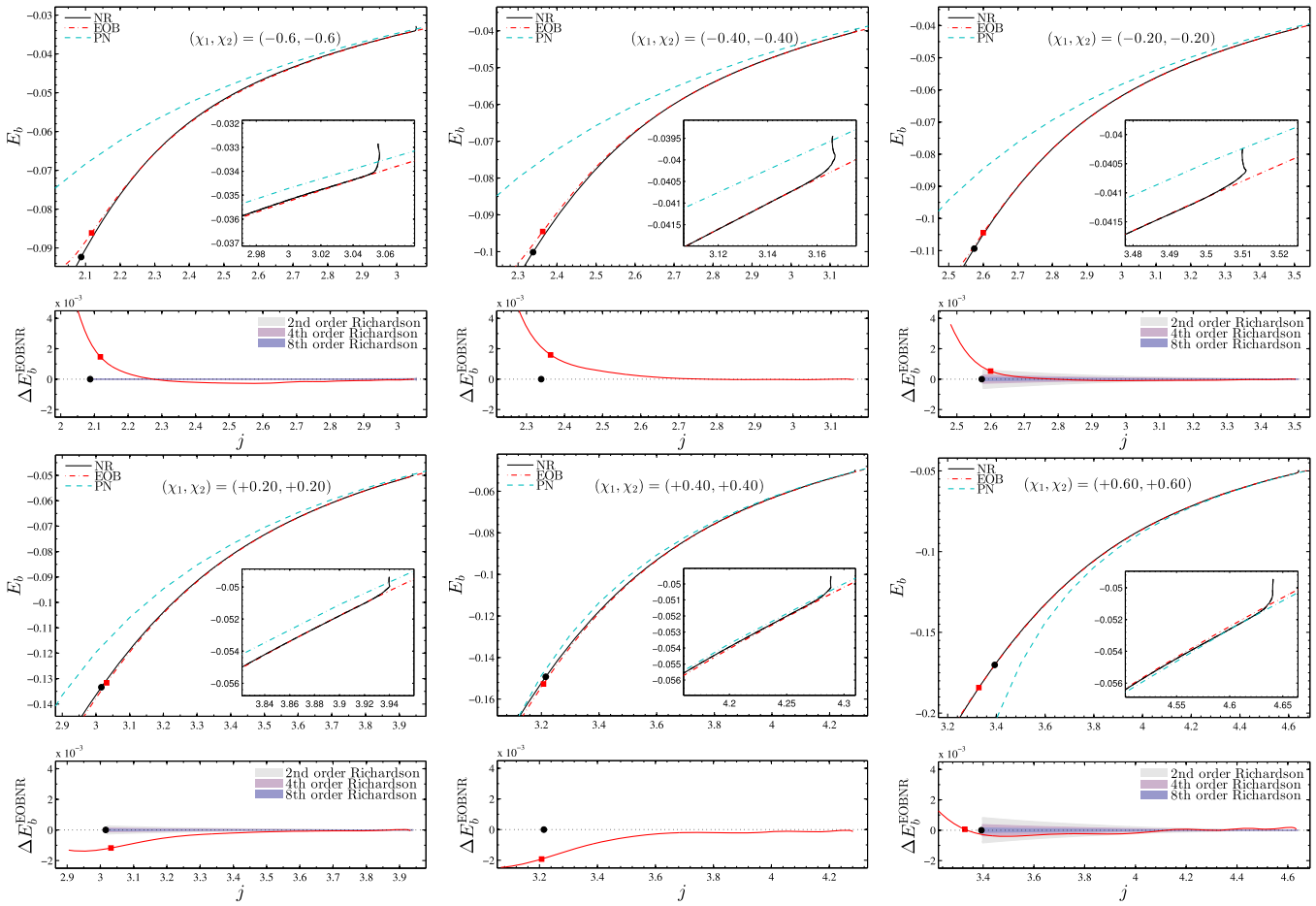

FIG. 11. Energy versus angular momentum curves for spinning equal-mass binaries with spin χ either aligned or antialigned to the orbital angular momentum, as obtained from Llama data. Good mutual consistency EOB/NR is found. The shaded area indicates an error bar estimate obtained by Richardson extrapolating three resolutions.

shift so as to have them as flat and as small as possible in the first part of the inspiral (see the Appendix for a fuller discussion). We choose here $(\Delta j^0, \Delta E_b^0) = (-1.3\times10^{-3}, 7.8\times10^{-4})$ for $\chi=-0.8$ and $(\Delta j^0, \Delta E_b^0) = (-1.3\times10^{-2}, 7\times10^{-4})$ for $\chi=+0.8$. Figure 13 (that refers to the $\chi=+0.8$ case) illustrates the effect that a good choice of Δj^0 has in centering around a zero averaged value the (eccentricity driven) oscillation in $\Delta\hat{\Omega}^{\rm EOBNR}(j)$. Figure 12 (bottom panels) shows how the use of the vectorial shifts substantially reduces the difference $\Delta E_b^{\rm EOBNR}$, making it compatible with the fourth-order extrapolation error bar.

Let us finally comment on the possible origin of the excessive initial drop in the $E_b(j)$ curve (visible in the insets of Fig. 12) yielded by the junk-radiation transient. We think it has to do with the under-resolution of the junk-radiation high multipoles ($4<\ell\leq8$) for the following reason: we noted that the energy loss during the junk transient yielded by the modes with $5\leq\ell\leq8$ is approximately *as large as* that for $2\leq\ell\leq4$ for $\chi_1=\chi_2=\pm0.8$; on the contrary, for the other configurations one always observes a sort of convergence of the junk radiation losses, with the higher multipoles contributing vertical drops that are progressively smaller than those due to the leading order modes. This makes us suspect that if it were possible to improve the accuracy of the higher-modes junk radiation one would be able to find the same straightforward (i.e., without shifts) EOB/NR consistency as for the case $-0.6\leq\chi\leq+0.6$. A more refined analysis of these issues (either employing higher resolution and/or starting the system at larger separations, so as to reduce the magnitude of the junk) is left to future work.

For the moment, to gain more confidence in our analytical model, as well as to gauge the evidence of systematic uncertainties in the NR data, we turn to explore the energetics of spinning binaries computed using SXS data.

B. Energetics of SXS spinning data

1. Equal-mass, spinning binaries: $-0.8\leq\chi\leq+0.8$

One of the crucial outcomes of the Llama/EOB comparison seen above is that, even when the separations are

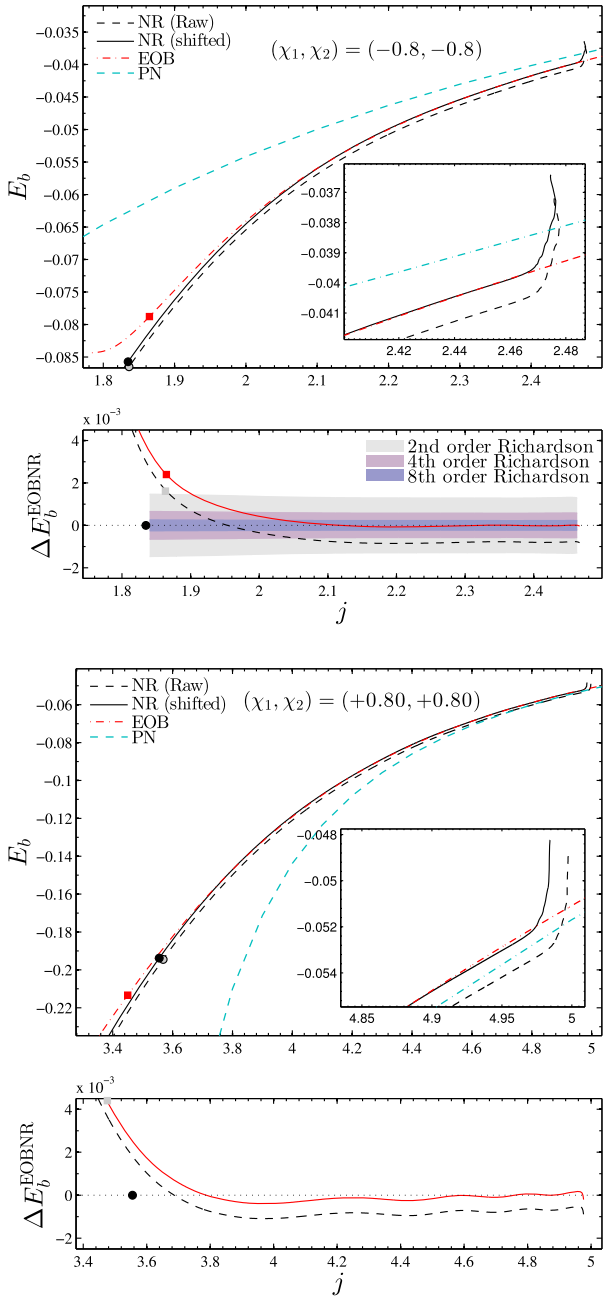

FIG. 12. Same as Fig. 11 (still for Llama data), but for the cases $\chi = \pm 0.8$. The black curves are obtained after shifting the raw data (dashed line) with the vector $(\Delta j^0, \Delta E_b^0)$ so as to recover a good EOB/NR consistency for large values of j. The Taylor-expanded PN curve is also added for comparison. The insets zoom on the initial (junk-related) drop in the $E_b(j)$ curve.

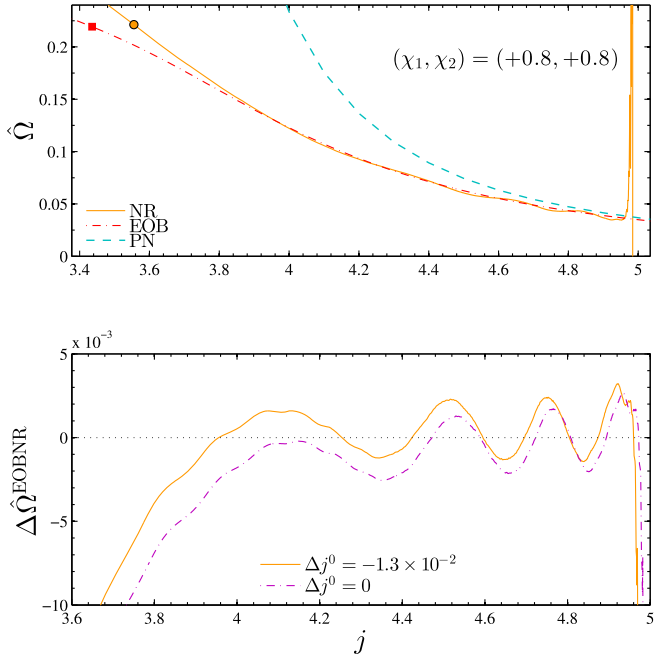

FIG. 13. Comparison between the analytical and numerical dimensionless orbital frequencies $\hat{\Omega}$ for the (Llama) case $\chi_1 = \chi_2 = +0.80$ in Fig. 12. The bottom panel shows how the difference $\Delta\hat{\Omega}^{\rm EOBNR}(j) = \hat{\Omega}^{\rm EOB}(j) - \hat{\Omega}^{\rm NR}(j)$ can be made to oscillate around zero by a proper choice of the angular momentum shift Δj^0.

relatively small, the NR energetics, represented by $E_b(j)$, quickly settles down to the EOB one after the initial junk radiation transient. This was clearly the case for $-0.6 \leq \chi \leq +0.6$. For $\chi = \pm 0.8$, we recovered approximately the same behavior after properly fixing a suitable vector shift $(\Delta j^0, \Delta E_b^0)$. Such a "convergence" of the NR $E_b(j)$ curve to the EOB one after the initial transition would, *a priori*, be expected to emerge even more clearly from any of the SXS data set at our disposal, since the initial separation between the black holes is much larger, so that the EOB curve should give an even better approximation to the NR one. However, in practice, as detailed in the Appendix, the SXS junk radiation is often rather large and tends to produce unphysical effects in the $E_b(j)$ curve. In some cases, the "raw" $E_b(j)$ NR curve is shifted in a region of the (j, E_b) plane which is clearly incompatible with the EOB prediction even in the early inspiral (see in particular Fig. 25 in the Appendix). As above, the problem is overcome by introducing a suitable shift vector $(\Delta j^0, \Delta E_b^0)$. More technical details, as well as the values of the shifts, are given in the Appendix.

Figure 14 illustrates the $E_b(j)$ comparison between the EOB predictions and the SXS data. The figure displays just the restricted sample of SXS configurations that overlaps with the Llama ones considered above, i.e. $\chi = (\pm 0.8, \pm 0.6, \pm 0.2)$. One sees that the result is compatible with the previous one, though improved in the following aspects: (i) the NR curves extend from larger values of j up to the final state corresponding to the mass and angular momentum of the final black hole. The final state, as read from the `metadata.txt` file in the SXS catalog, is also indicated by the grey square marker in the plots; (ii) due to the improved accuracy of NR data, the differences between EOB and NR merger states (indicated

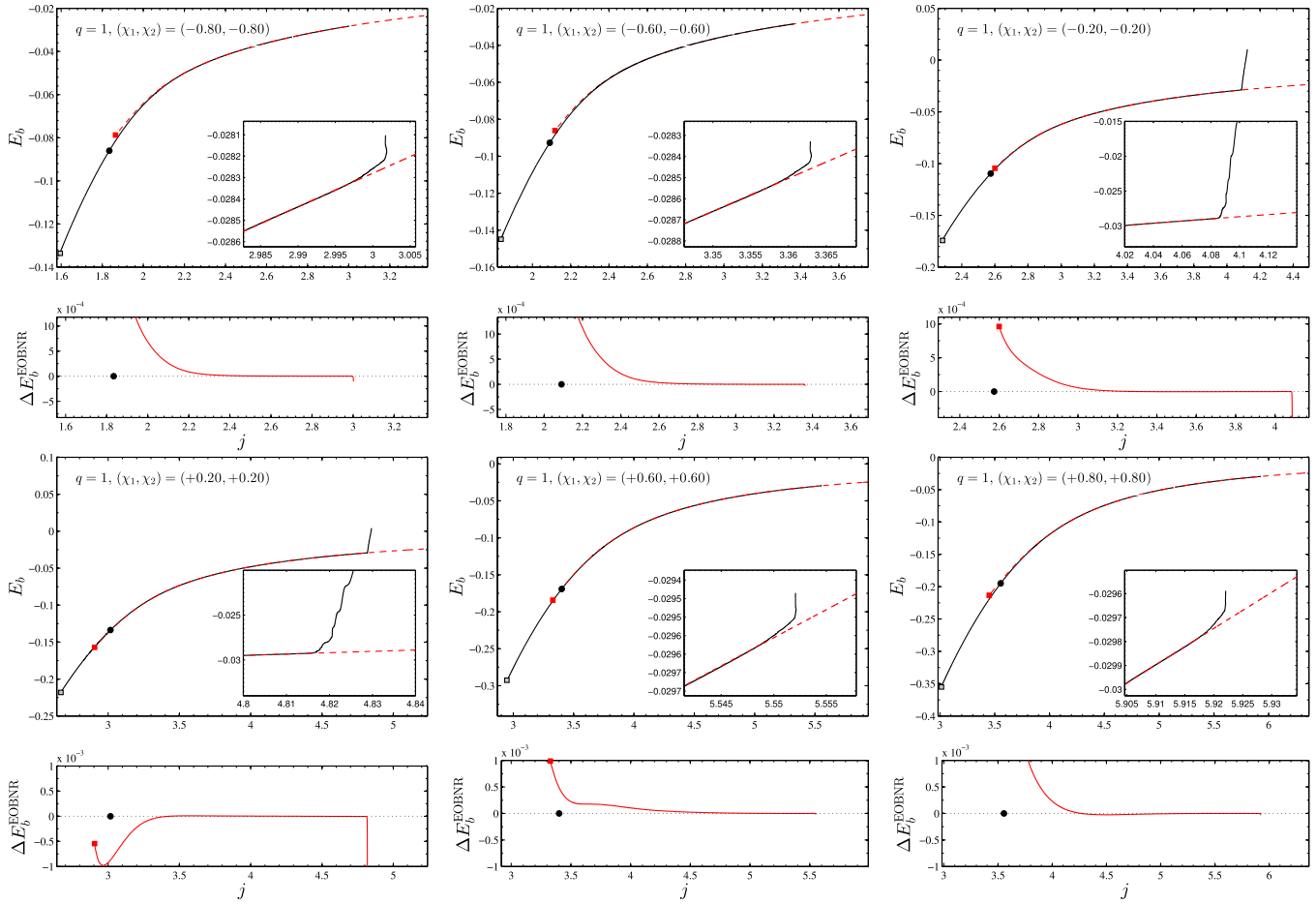

FIG. 14. Energy versus angular momentum curves for equal-mass binaries with spin χ either aligned or antialigned to the orbital angular momentum as obtained from SXS data set. This cross-checks the above comparison with Llama data.

by markers in the plots) are visibly smaller (and more homogeneous) than with Llama data. Compare in particular the case ± 0.2. Generally speaking, the EOB and NR curves are seen to progressively separate as the spin becomes negative and large. Still, the final merger states are closer when the spin is negative than when the spin is positive. Such differences are typically larger than the numerical error, when available (shaded region in the plot): this suggests that the performance of the EOB model should be improved close to merger when the BHs are spinning.

The insets in the panels of Fig. 14 are close-ups of the initial junk-radiation-transient parts. Note that the magnitude of the junk radiation transient [and thus of the shift $(\Delta j^0, \Delta E_b^0)$ that has to be applied] is very different depending on the configuration. The cases $\chi = \pm 0.2$ are particularly remarkable. For them, rather large vectorial shifts need to be applied to reconcile the NR curve with both the EOB at low frequencies and the final state.

The difference between Llama and SXS merger states is rather small in absolute value ($\sim 10^{-4}$), and compatible with the expected level of conservation of energy and angular momentum in the Llama code (see Table 2 of Ref. [51]). Note that the energy conservation in SXS data is on average more accurate by 2 orders of magnitude (see Table II of Ref. [22]). The compatibility among NR merger data is highlighted in Fig. 15: the figure plots the functions $E_b^{\rm mrg}(\chi)$ and $j^{\rm mrg}(\chi)$ (including also extremal spin values, see below); Llama and SXS data are hardly distinguishable on this scale. The SXS NR merger states $E_b^{\rm mrg}(\chi)$ and $j^{\rm mrg}(\chi)$ shown in the picture can be accurately fitted with quadratic polynomials in χ,

$$E_{b,\rm SXS}^{\rm mrg}(\chi) = -0.035546\chi^2 - 0.070311\chi - 0.119444, \quad (23)$$

$$j_{\rm SXS}^{\rm mrg}(\chi) = -0.180948\chi^2 + 1.068176\chi + 2.805593. \quad (24)$$

The figure also summarizes the performance of the EOB model at merger (the corresponding points are indicated by red, empty squares), highlighting that the EOB/NR agreement between merger states, which is best when $\chi = 0$, slightly worsens when $\chi < 0$ and worsens more markedly when $\chi > 0$, and especially when $\chi \to 1$. Such a disagreement calls for improvements in the analytical EOB model that will be undertaken in future studies. We recall however

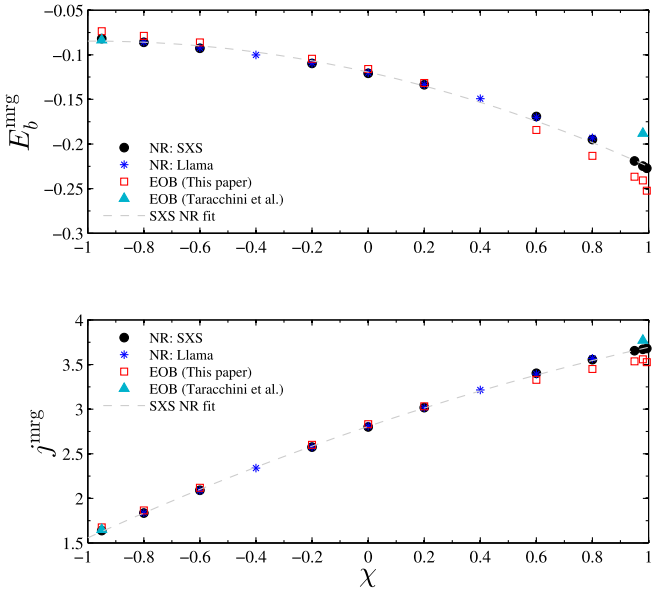

FIG. 15. Equal-mass, equal-spin case. Comparison between EOB and NR merger quantities, binding energy (top) and angular momentum (bottom).

that, despite such discrepancies in the energetics, the *phasing* provided by the EOB model discussed here is in excellent agreement with NR data, as illustrated by the dephasing and unfaithfulness data of Table I.

2. Extremal spins and comparison with the results of Taracchini et al. [11]

Let us finally analyze in detail some (equal-mass, equal-spins) quasiextremally spinning binaries that are present in the SXS catalog, $\chi = -0.95$, $\chi = +0.98$ and $\chi = +0.994$, the highest spin value simulated so far. We recall that before the SXS catalog became public, data with $\chi = -0.95$ and $\chi = +0.98$ were used by Taracchini *et al.* [11] to test the phasing and energetics of their EOBNR model. We note that the EOB model of Ref. [11] differs in many aspects from the one we are presenting here. Since we have presented a new computation of $E_b(j)$ taking advantage of an improved understanding of various subtleties, we think it is pedagogically useful to compare and contrast our new NR-based results with both the EOB and the NR curves of Ref. [11]. The latter data were kindly given to us by Taracchini and Buonanno. The result of our comparison is illustrated in Fig. 16. Each top panel of Fig. 16 contrasts four curves: (i) our newly computed NR curve, using a suitable vectorial shift (black); (ii) our new EOB curve (red, dashed); (iii) the EOB curve of Ref. [11] (light blue); (iv) the NR curve of Ref. [11] (dot-dashed, magenta). In addition, in the bottom panel of Fig. 16, we show the corresponding differences together with the NR numerical uncertainties, depicted as a shaded grey region. Such NR uncertainties were computed by the following procedure: (i) for the two highest resolutions available, we determined

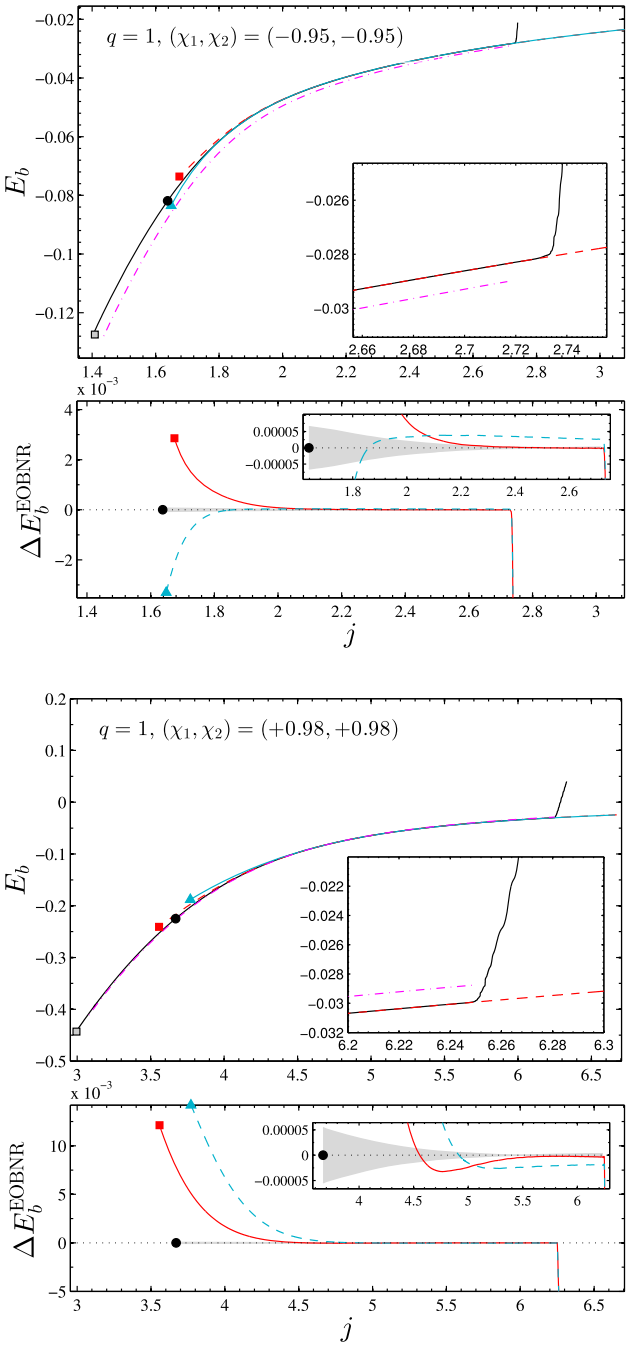

FIG. 16. Energetics in the extremally spinning case: comparison with the EOB and NR data of Ref. [11]. Markers indicate the merger for each data set (except the NR data of Ref. [11]): NR (red); EOB model of Ref. [11] (light-blue); our EOB model (red). The shaded area gives an estimate of the numerical uncertainty. Both EOB models are consistent among themselves and with the NR curves computed in this paper. For $\chi = +0.98$ our EOB model is closer to NR than the EOB model of [11], while the reverse is true for $\chi = -0.95$.

the corresponding $E_b(j)$ curves and the related vectorial shifts $(\Delta j_0, \Delta E_b^0)$; (ii) we took the difference between the so computed highest and second highest resolution data, $\Delta E_b^{\rm NRNR}$; (iii) the shaded region corresponds to $\pm\Delta E_b^{\rm NRNR}$.

The uncertainty we obtain in this way looks rather small: it is $\sim 10^{-6}$ for large values of j, to grow up to a mere $\sim 10^{-4}$ towards merger.

A careful inspection of this figure tells us that:

(i) The energetics yielded by our EOB model is consistent with extremally spinning NR data, and exhibits the continuation of the trend we found above for $|\chi| \leq 0.8$. For both spins, our EOB curves are slightly *above* the NR ones close to EOB merger.

(ii) Regarding the comparison with the EOB model of Ref. [11] we note first that the two EOB's are perfectly consistent among themselves (and with the NR data) during most of the early inspiral. The two EOB models start differing among themselves (and with NR) when getting close to merger. For $\chi = -0.95$ the EOB model of Ref. [11] gives a better approximation to the final state than our model; on the contrary, for $\chi = +0.98$ our model performs quantitatively better near merger. Note that, in spite of these differences in energetics, the waveforms delivered by both EOB models agree well with NR data within the NR uncertainty [11].

(iii) On the same plot, we superpose the NR $E_b(j)$ curves presented in Ref. [11] (dashed lines; red). The curves exhibit significant differences with both EOB models already in the early inspiral. Moreover their end point (after merger and ringdown) differs from the actual final mass and angular momentum of the BH (as extracted from the SXS file `metadata.txt` and displayed in the figure). By contrast we note that we determined the additional, needed, final shifts taking care that this last point (computed with high accuracy) approximately (10^{-4} level) coincides with the final point of the $E_b(j)$ curve. No details were given in Ref. [11] on how their $E_b(j)$ curve was computed.

(iv) As a side remark, we note that the red and light-blue curves in each inset of Fig. 16 differ at the $\sim 10^{-5}$ level. Since both curves were obtained subtracting the corresponding EOB to the same NR curve, this 10^{-5} level essentially quantifies the analytical difference, in the early inspiral, between the conservative dynamics of our EOB model and that of SEOBNRv2.

To conclude, Fig. 17 illustrates the EOB/NR comparison for the highest value of the spin available, $\chi = +0.994$. The numerical uncertainty, computed as outlined above, is again rather small, as it does not exceed the 10^{-4} level towards merger. The performance of the EOB in this case is essentially analogous to the $\chi = +0.98$ case illustrated above, though with a slightly larger displacement between the EOB and NR merger states.

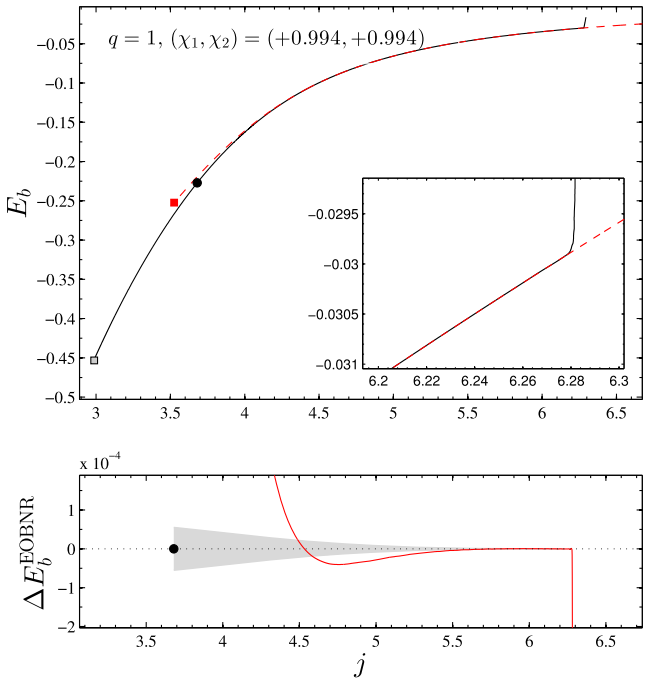

FIG. 17. EOB/NR comparison for $q = 1$, $\chi_1 = \chi_2 = +0.994$ (bottom), the highest spin simulated so far. The NR uncertainty (shaded region) is obtained by taking the difference between the data at the two highest resolutions after determining the corresponding vectorial shifts $(\Delta j^0, \Delta E_b^0)$.

3. Unequal-mass, spinning binaries

We conclude this survey of EOB/NR energetics comparison by also discussing explicitly a few representative configurations with both unequal masses and unequal spins. The comparison is illustrated in Fig. 18, which collects six representative configurations, notably the high-mass-ratio ones $(8, \pm 0.50, 0)$. We show here explicitly those cases where only one of the two black holes is spinning, since in these cases we have enough resolutions to compute error bars. The two cases $(3, -0.50, -0.50)$ and $(3, +0.50, +0.50)$ yield equivalent results. The numerical uncertainties, computed as in the previous section, are represented by light-gray shaded areas: notably, these error bars are compatible with the extremally spinning cases discussed above, i.e. about 2×10^{-4} towards merger (we expect to get similar results also for the other configurations). Generally speaking, we see here the same features we were finding in the equal-mass, equal-spin cases shown in Figs. 14, 16 and 17. In particular, one sees that (i) when the BH spin is positive, the EOB model predicts values of the merger states that are slightly smaller than what they should be. This occurs independently of the mass ratio. Similarly, (ii), when the BH spin is negative, the EOB predicts values that are slightly, but significantly, higher than the NR prediction. If both black holes are spinning, these effects remain qualitatively the same, though

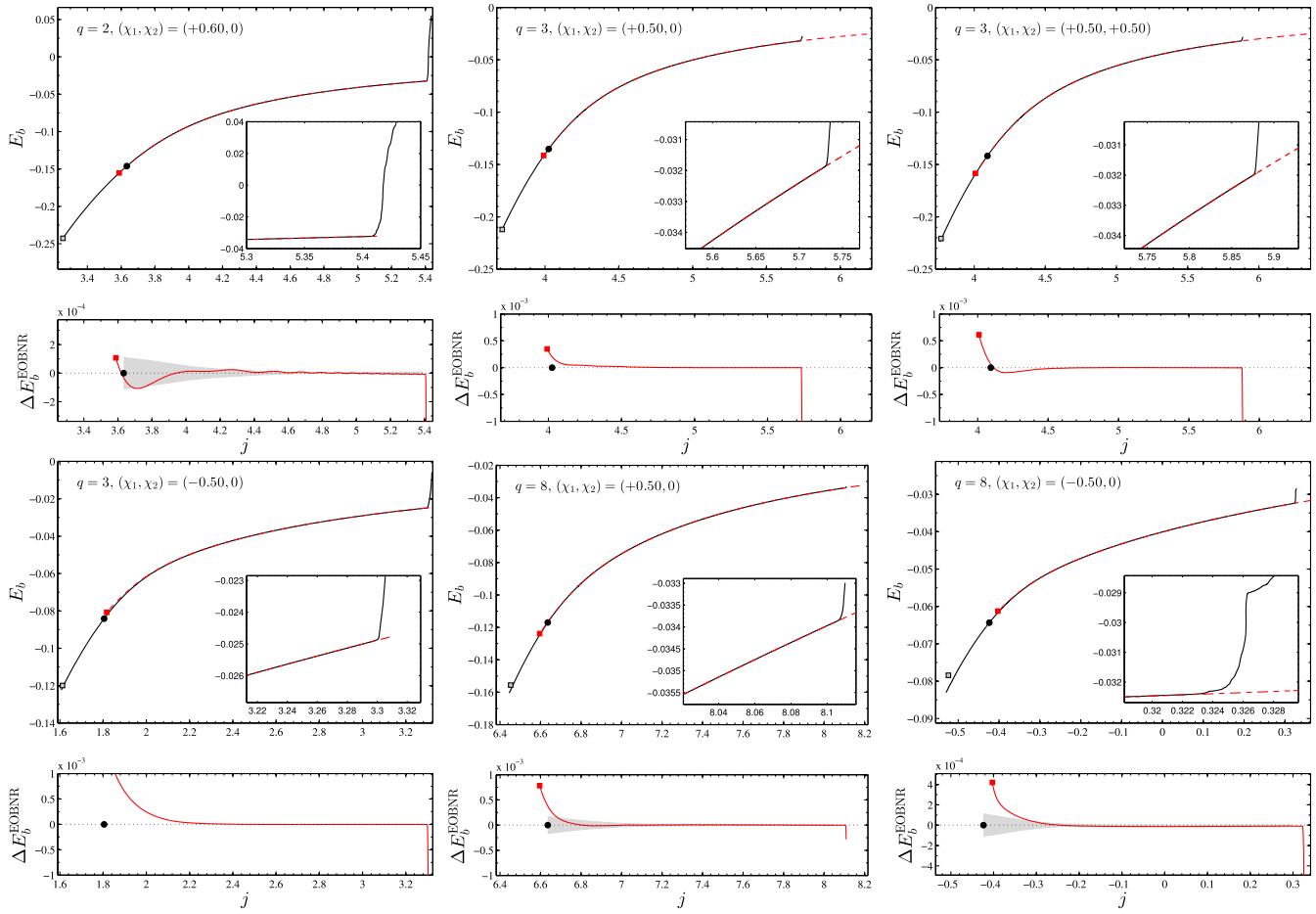

FIG. 18. Energetics comparison for a selected sample of unequal-mass, unequal-spin binaries. The EOB/NR compatibility is essentially comparable to the equal-mass results shown in Figs. 14, 16, 17.

quantitatively are slightly magnified. In other words, the $E_b(j)$ analysis seems to indicate that the current EOB model is slightly overestimating the magnitude of the spin-orbit interaction. Note however that the $E_b(j)$ diagnostics is here magnifying a difference that corresponds to a very small part (near merger) of the time-domain waveform. Let us only note here that this shows the usefulness of the $E_b(j)$ diagnostics for understanding subtle physical effects in the spin-orbit interaction that cannot be appreciated by just inspecting the phasing.

VII. PRELIMINARY COMPARISON OF THE TWO EXISTING SPINNING EOB MODELS

Let us finally highlight some differences between the analytic structure of our EOB model and that of Ref. [11] by comparing some crucial quantities that enter the construction of the models.

As a first example, we focus on the $q = 1$, nonspinning case. Figure 19 compares three $A(r)$ curves: our NR tuned $A_{\rm orb}(r)$ curve, with a_6^c given by Eq. (5); the $A(r)$ of Ref. [11], calibrated to the same sample of nonspinning NR waveform data we used here; and the Schwarzschild $A(r)$. The markers on the plot indicate the location of the (adiabatic) "light-ring," defined as the peak of the effective "photon-potential" $A(r)/r^2$ (corresponding to $r = 3M$ for the Schwarzschild metric). Let us first note a qualitative difference: our choice of resumming the Taylor-expanded A function with a Padé (1,5) approximant entails that our function $A_{\rm orb}(r)$ vanishes at $r = 0$. This is qualitatively different from $A^{\rm Tar}(r)$, whose (non Padé) resummation is chosen so as to impose the existence of a horizon at a nonzero value of r. As a consequence, our radial potential is more repulsive than $A^{\rm Tar}(r)$ when $r \lesssim 2$.

From the quantitative point of view, let us note that our $A_{\rm orb}(r)$ and $A^{\rm Tar}(r)$ are rather close up to the light-ring of $A^{\rm Tar}(r)$. Their difference (up to their light-ring location, blue dot) ranges between -3×10^{-3} and approximately 7×10^{-3} at the light-ring point. Although such differences look small, let us emphasize that, as discussed in Ref. [29], these differences are large enough to make the two potentials belong to *different* "equivalence classes," i.e. to yield significantly different conservative dynamics. Indeed, Ref. [29] found that one needed differences smaller than the 10^{-4} level to lead to indistinguishable dynamics.

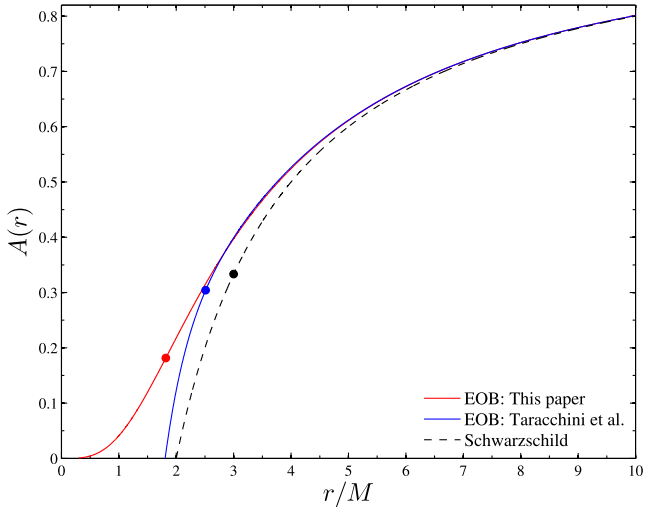

FIG. 19. Comparison between EOB radial potentials $A(r)$: the Schwarzschild case is contrasted with the $q=1$, nonspinning function of Taracchini *et al.* [11] and the Padé-resummed, NR completed one of this paper, Eq. (4), with $a_6^c(\nu)$ given by Eq. (5). The marker indicates the location of the "light-ring," i.e. the peak of the effective "photon-potential" $A(r)/r^2$ (located at $r=3M$ for Schwarzschild).

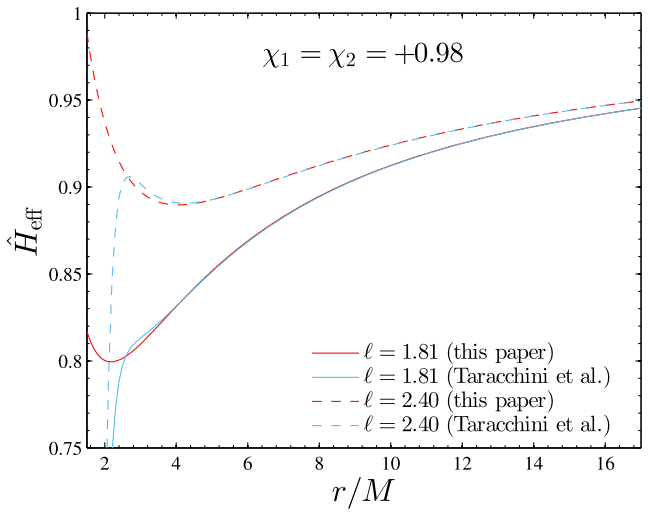

FIG. 20. Comparison between effective Hamiltonians $\hat{H}_{\rm eff}(r,\ell,\chi)$ obtained by using our EOB spinning model and the one of Ref. [11] for $\chi=+0.98$ and for two values of the dimensionless orbital angular momentum ℓ. The value $\ell=1.81$ corresponds to the merger location of the blue curve in Fig. 19. For $\ell=1.81$ our effective potential is such that the system is still inspiralling.

As a second example of comparison between our EOB dynamics and that of Ref. [11] we compare in Fig. 20 the dimensionless effective potential $\hat{H}_{\rm eff}(r,\ell,\chi)$ (including spin-orbit and spin-spin interactions, but with $p_{r_*}=0$), for $\chi=\chi_1=\chi_2=+0.98$ and two representative values of the dimensionless orbital angular momentum ℓ. For the value $\ell=2.40$, both effective potentials exhibit a local minimum, corresponding to a stable circular orbit. On the other hand, for $\ell=1.81$ (which corresponds to the merger location of the blue curve in Fig. 19) the model of Taracchini *et al.* no longer allows for a stable circular orbit, while ours still does. In other words, our dynamics is still inspiralling, while that of Ref. [11] is already "plunging." Note that for $\chi=\chi_1=\chi_2=+0.98$ we have seen above that our energetics is closer to the NR one. It should, however, be kept in mind that we are here comparing two conservative dynamics while the real EOB dynamics is also (especially near merger) strongly modified by radiation reaction effects.

VIII. CONCLUSIONS

In this paper we have presented a new NR completion of the spinning, nonprecessing, EOB model introduced in Ref. [1].

Our new EOB model uses only *two* flexibility[6] parameters, one for the nonspinning sector $a_6^c(\nu)$, and one for the spinning sector $c_3(\tilde{a}_1,\tilde{a}_2;\nu)$. We have calibrated the functions $a_6^c(\nu)$ and $c_3(\tilde{a}_1,\tilde{a}_2;\nu)$ by comparing EOB predictions to a large sample (∼50) of NR data waveforms computed with two different numerical codes (Llama and SpEC). This calibration is done (for every step) through a simple one-parameter search by requiring that the EOB/NR time-domain phase difference (after alignment) stays within NR uncertainty up to merger. This is achieved in two steps: the function $a_6^c(\nu)$ is determined first by using nonspinning data; then the single remaining flexibility parameter $c_3(\nu;\tilde{a}_1,\tilde{a}_2)$ is determined by using spinning data.

The EOB/NR comparison is done both for phasing and energetics [gauge-invariant relation $E_b(j)$ between binding energy and angular momentum].

Our main results are the following:

(i) The $\ell=m=2$ GW phasing performance of our new spinning EOB model (measured both by the time-domain EOB/NR phase difference and through faithfulness computations) is at least as good as that of the most recent version of the spinning EOBNR model developed by the group of Buonanno [10,11,48]. To quantitatively assess the quality of our unfaithfulness results, we display in Fig. 21 a histogram of the maximized-over-mass values of the unfaithfulness,[7] $\bar{F}_{\rm max}\equiv\max_M(\bar{F}(M))$, over the entire sample of SXS waveforms we use.

[6]Let us recall that the idea of using the "flexibility" of the EOB formalism to determine effective values of yet uncomputed higher-order analytical functional parameters [such as $a_6(\nu)$] by fitting EOB predictions to NR data was introduced, and first implemented, in Ref. [52].

[7]We recall that those unfaithfulnesses are only integrated over the NR frequency range.

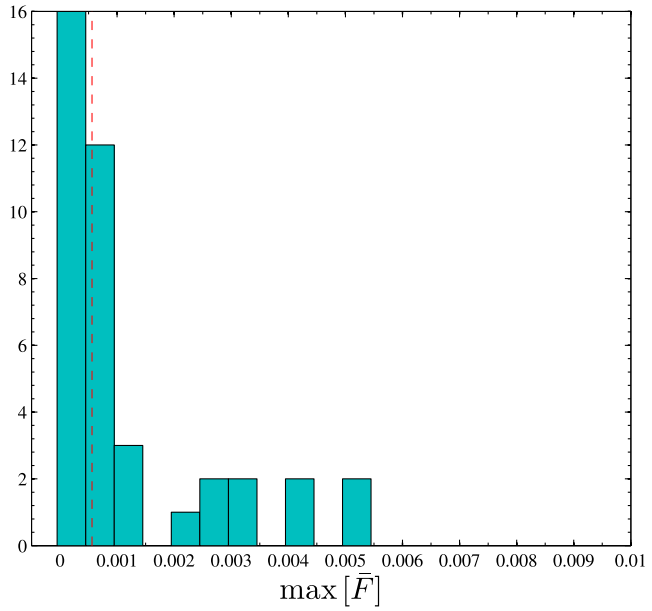

FIG. 21. Maximum value of the EOBNR unfaithfulness $\bar{F}$ (listed in Table I) for all SXS data set considered. The vertical line indicates the median of the histogram, corresponding to 0.00056105.

Note that the histogram is skewed towards very small values of $\bar{F}_{\max}$, with a median value equal to 0.00056105 (see vertical line on the figure). It is interesting to note that $\bar{F}_{\max} \lesssim 0.003$ for all data except for the case $(q, \chi_1, \chi_2) = (1, -0.50, 0)$ and the near-extremal spin $q = 1$ data sets with $\chi = \chi_1 = \chi_2 = (+0.98, +0.99, +0.994)$. For the latter data sets, note that $\chi = +0.99$ and $\chi = +0.994)$ both yield $\bar{F}_{\max} \approx 0.005$, while $\chi = 0.98$ yields $\bar{F}_{\max} \approx 0.0042$.

When comparing the mass dependence of $\bar{F}$ in our Fig. 9 with the corresponding quantity displayed in Fig. 1 of Ref. [11] one notices the following facts: (i) our $\bar{F}(M)$ is, for all values except a few, maximal around $M = 20M_\odot$ and then monotonically decreases as M increases. By contrast, the mass dependence of the $\bar{F}(M)$ of Ref. [11] is quite different: either it increases monotonically from $20M_\odot$ to $200M_\odot$ or it has a local maximum. We attribute the mass behavior of our $\bar{F}(M)$ to the new, more accurate attachment of the ringdown part [14] which we have implemented in our model. (ii) In Fig. 1 of [11] we spot *two* outliers with $\bar{F}_{\max} \approx 0.01$: one is SXS:BBH:0065, with $q = 8$ $(\chi_1, \chi_2) = (+0.5, 0)$; the other outlier of Ref. [11] is SXS:BBH:0152, with $q = 1$, $\chi_1 = \chi_2 = +0.6$. We stress that our corresponding values $\bar{F}(M)$ remain below 10^{-3}, as displayed in Fig. 9.

(ii) We have presented the first systematic, accurate computation of $E_b(j)$ curves from SXS and Llama data of nonprecessing, spinning (or nonspinning) configurations. Our results significantly improve previous attempts to do so and give us a reliable target for EOB calibration, that complements the usual phasing analysis.

For the nonspinning sector of the model, the inspection of the NR $E_b(j)$ curves led us to decide that the choice $\mathcal{F}_{r_*} = 0$ (which was already used in early EOB works [35,36]) leads to a good EOB/NR agreement between the corresponding energetics, at the 10^{-4} level up to merger. We hope to further study (both analytically and numerically) the role of the radial part of radiation reaction, and its influence on Schott terms. The results presented in Figs. 4 and 5 have shown the potential of SXS data for very accurate investigations of energetics in coalescing black hole binaries.

The $E_b(j)$ NR curves were computed using two different sets of numerical data, one by the Llama code and the other by the SpEC code. We solved several subtle issues related to the computation of $E_b(j)$ from SXS data. In particular, for the cases of extremal spins $\chi_1 = \chi_2 = -0.95$ and $\chi_1 = \chi_2 = +0.98$, we showed that the corresponding NR curves presented in Ref. [11] were inconsistent both with the NR final state (as provided in the SXS files itself) and with early inspiral EOB predictions. This allowed us to meaningfully compare, for the first time, extremal-spin NR data both to our EOB model and to the one of Ref. [11]. The main outcomes of this comparison are (i) for $\chi = +0.98$, the energetics predicted by our model is closer than that of the model of Ref. [11], to the NR one, during the late inspiral and near merger; (ii) for $\chi = -0.95$, the opposite is true, with the model of Ref. [11] being closer than ours to the NR values near merger.

(iii) The EOB model we are presenting here is analytically simpler than the one of Ref. [11], while it performs at a comparable accuracy (which is demonstrably better in some situations, e.g. the case of SXS:BBH:0152 data). The structural simplicity of our spinning EOB model is such that it is easy to recalibrate it if the needs occurs, e.g. in the case that further linear-in-ν corrections to the gyro-gravitomagnetic ratios (G_S, G_{S_*}), as defined in Paper I, are introduced. Different analytical expressions would imply a different determination of the function $c_3(\tilde{a}, \tilde{a}; \nu)$. In addition, it is straightforward to incorporate tidal effects in the model simply by augmenting the pure orbital A function with the tidal potential recently determined in Ref. [37] so as to build a BNS (or BHNS) spinning EOB model. The performance of such a tidal, spinning, EOB model, as well as its eventual calibration, will have

to be carefully assessed against state-of-the-art NR simulations of spinning NS binaries [53].

(iv) The preliminary comparison given here between the performances of our model and the EOB model of Ref. [11] was purely based on information that was either given to us or that was extracted from the literature. We also emphasized some of the structural differences between these two spinning EOB models: (i) In Fig. 19 we contrasted the two different EOB $A(r)$ radial potentials for $q=1$ nonspinning black holes; and (ii) in Fig. 20 we contrasted the two effective Hamiltonians $\hat{H}_{\rm eff}(r)$ for $q=1$ and $\chi=+0.98$. The differences are non–negligible and are probably partly responsible of the different performances of the two EOB models versus the NR $E_b(j)$ curve for $\chi=+0.98$. We hope that it will be possible to perform soon a more detailed comparison between the two spinning EOB models, notably by directly comparing waveforms. We think that a synergetic effort dedicated to transferring the best features of each EOB model into a new model for spinning binaries will be crucial for the forthcoming gravitational wave astronomy.

ACKNOWLEDGMENTS

We thank Andrea Taracchini, Alessandra Buonanno and the other authors of Ref. [11] for sharing with us the NR and EOB $E_b(j)$ curves for $\chi=-0.95$ and $\chi=+0.98$; Michael Puerrer for useful comments on the first version of the manuscript; Sascha Husa for assistance in computing low eccentricity initial data; and Simone Balmelli for help with generating the data of Fig. 20. We finally thank Michael Boyle for having computed for us the data of Fig. 23 so as to approximately remove the drift of the center of mass. C. R. acknowledges support by NASA through Einstein Postdoctoral Fellowship Grant No. PF2-130099 awarded by the Chandra X-ray center, which is operated by the Smithsonian Astrophysical Observatory for NASA under Contract No. NAS8-03060. Computations were performed using resources of the NASA High-End Computing (HEC) Program through the NASA Advanced Supercomputing (NAS) Division at Ames Research Center and NSF XSEDE (allocation TG-MCA02N014 and TG-PHY100033). Additional computations were performed on the Caltech computer cluster "Zwicky" (NSF MRI award No. PHY-0960291).

APPENDIX: COMPUTING $E_b(j)$ USING SXS WAVEFORMS

In this appendix we discuss in detail the procedure we adopt to compute the function $E_b(j)$ using SXS NR data. First, in Sec. 1 we contrast SXS with Llama data and highlight some (minor) unsatisfactory features of the SXS waveforms. The actual $E_b(j)$ computation is detailed in Sec. A 2 below.

1. Unphysical effects in the $q=1$, SXS multipolar waveforms

For an equal-mass binary, with equal (aligned or antialigned) spins, the fact that the system is symmetric by exchange of the two black holes ensures that all multipoles with $m=$ odd have to vanish. We verified that this is essentially the case for all Llama simulations at our disposal: in the time plots of these multipoles, only uncorrelated noise is found. On the contrary, a careful inspection of SXS data led us to the discovery that the $m=$ odd multipoles have amplitudes, which are small but which are not just uncorrelated noise. Rather they qualitatively show some sort of chirping structure present in the actual physical modes with $m=$ even. This is illustrated in Fig. 22 for the case $q=1, \chi_1=\chi_2=+0.6$, corresponding to data set SXS:BBH:0152 of the SXS catalog. The figure contrasts the SpEC modes (top panel) with the corresponding Llama modes (bottom panel). One immediately sees the striking qualitative difference between the two independent simulations of the same physical system. Though, the amplitude of these modes is so small that it does not have any practical influence on the $E_b(j)$ computation,[8] it is interesting to briefly point out the impact of two physical effects on shaping the multipolar structure of the modes: (i) the motion of the center of mass (CoM) of the system and (ii) the (tiny) asymmetry of the (nominally symmetric) initial binary configuration.

The effect of the motion of the CoM due to residual linear momentum in the initial data has been investigated in some very recent work [54,55]. Notably, Ref. [55] introduced a method to eliminate such residual momentum from the initial data, so that future SXS waveforms will be amended of such systematic uncertainty. However, as emphasized by Boyle [54], the waveforms currently present in the SXS catalog *are not* expressed in the CoM frame (as are the EOB ones) and this introduces systematic uncertainties that should be removed. As a matter of fact, Ref. [54] (that appeared while this paper was under evaluation) proposed a way to remove the effect of the CoM drift from the waveforms. We asked Boyle to kindly apply his removal procedure to the SXS:BBH:0152 configuration we are discussing here. His result is shown (with his permission) in Fig. 23. One sees that the secular growth of the mode amplitudes is visibly reduced (though it is not

[8]We have analyzed what happens if the $m=$ odd modes are put to zero. We find that the resulting small difference (mainly coming from the $m=$ odd junk radiation) can be absorbed by modifying the vectorial shift $(\Delta j^0, \Delta E_b^0)$ mentioned in the main text and discussed below. In practice, all our $E(j)$ curves are computed using the full multipolar information at our disposal including multipoles up to $\ell=m=8$.

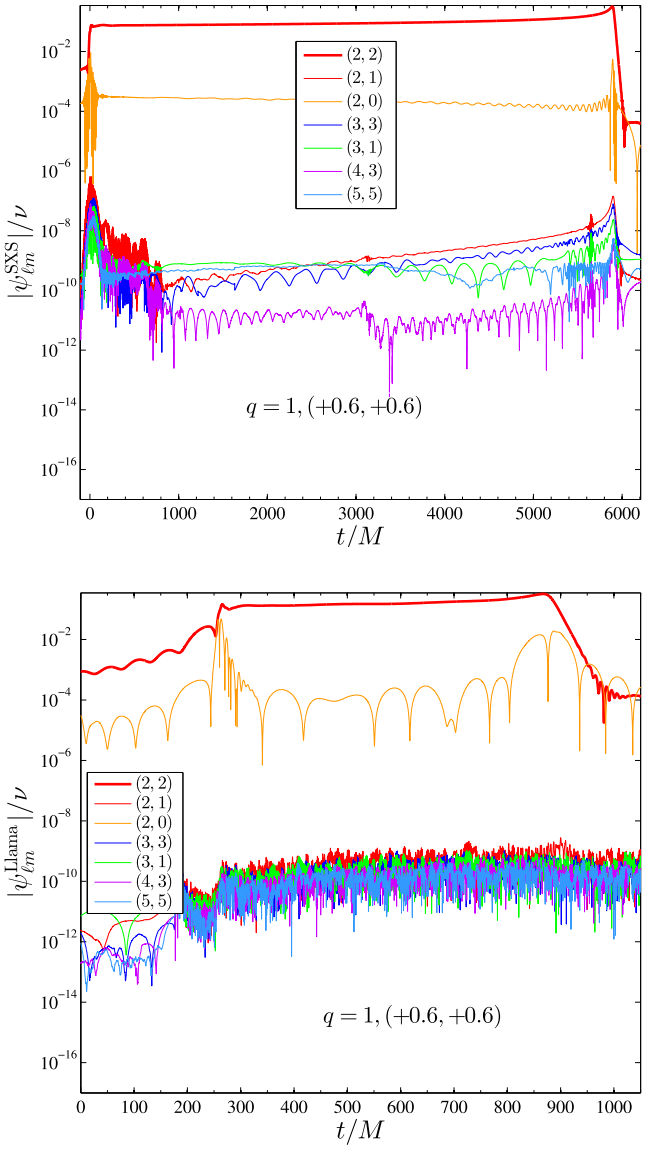

FIG. 22. Analysis of the subdominant multipoles of $q = 1$ SXS waveforms (top panel). The figure compares the amplitudes of various subdominant multipoles to the $\ell = m = 2$ one. The multipolar amplitudes with $m =$ odd grow in time likewise the dominant one. This effect (that is found in all $q = 1$ data) is (partly) related to the motion of the center of mass and to residual tiny asymmetries in the initial data, as discussed in the text. It is, however, absent in the corresponding Llama waveform data (bottom panel).

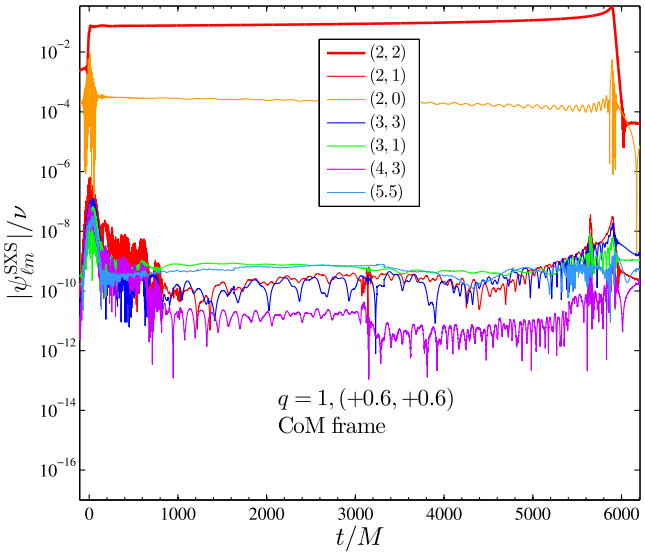

FIG. 23. The same SXS multipolar waveform of Fig. 22 after Boyle removed the drift of the CoM using the procedure of Ref. [54]. The subdominant multipolar amplitudes look flatter than in Fig. 22 and qualitatively closer to the Llama ones.

completely removed, especially towards merger). This is particularly visible for the (2,1) mode, where the trend visible in Fig. 22 is replaced by randomlike oscillations. Globally, the amplitude of the modes is rather constant, with less structure than before, and visually more consistent with the outcome of the Llama simulation. Improvements in the determination of the CoM frame of a NR simulation may flatten the $m =$ odd modes even further.

Let us now turn to estimating the effect on the $m =$ odd multipoles due to the tiny asymmetry present in the NR initial data. Inspecting the file `metadata.txt` of data set SXS:BBH:0152, one finds that initial masses and initial spins are actually slightly different; i.e., one has $m_1 = 0.499999998745987$, $m_2 = 0.499999997467155$ and $\chi_1 = 0.599963311735964$, $\chi_2 = 0.599963312827750$. These values of the initial masses yield $\nu = 0.25$ at machine precision, though $X_1 - X_2 = (m_1 - m_2)/M = 1.278831984752316 \times 10^{-9}$. We then estimated the impact of these tiny asymmetries by running an EOB simulation with precisely these spin parameters and this value of $X_1 - X_2$ entering the subdominant odd-parity modes. The multipolar amplitudes of the EOB waveform computed with these choices are exhibited in Fig. 24: one sees that during inspiral, where the analytical (EOB, resummed) waveform is highly reliable, the amplitude of subdominant modes is from 1 (for the ψ_{21} mode) to approximately 2 (for the ψ_{43} mode) orders of magnitude smaller than the corresponding SXS multipoles in the CoM frame. In Fig. 24 we also added the SXS (2,1) mode, in the CoM frame, to ease the comparison. This finding suggests that the magnitude of the subdominant multipolar amplitudes we see in Fig. 23 is only partially due to the asymmetry in the initial data and that other effects are present. In any case, since the analysis we did here confirms that the effects of the asymmetries are practically negligible, we are entitled to ignore them and consider exactly symmetric initial data for the EOB evolutions.

Finally, let us note in passing that $|\psi^{\rm EOB}_{21}| \approx |\psi^{\rm EOB}_{33}|$ up to merger, likewise the corresponding SXS multipoles in the

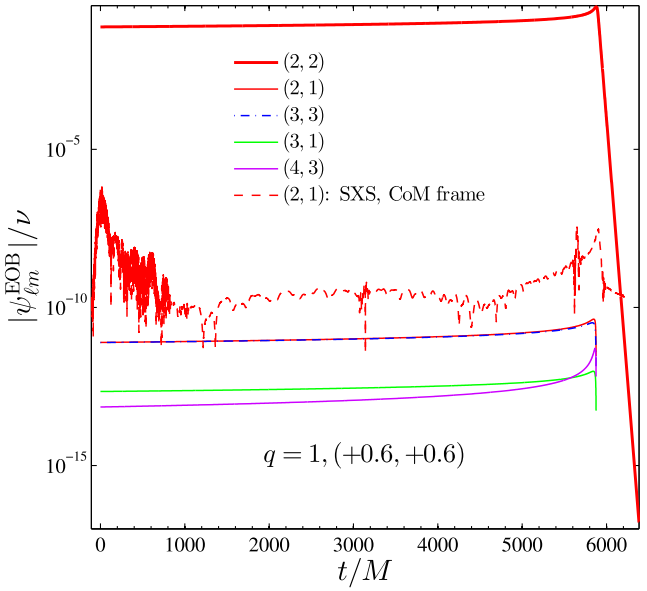

FIG. 24. Investigating the effect of tiny asymmetry in the initial data at the level of EOB waveform. The (2,1) mode of Fig. 23 is also included for visual comparison. The asymmetry in the initial data is not sufficient to fully explain the magnitude of the subdominant modes in the data of Fig. 23.

CoM frame in Fig. 23. This result contrasts with the top panel of Fig. 22, where the (2,1) and (3,3) modes were not coinciding, and gives further evidence of the need of removing the effects of the CoM motion from the SXS waveforms. Although the numerical effects we are pointing out here are small and practically negligible for the equal-mass configurations, they may not be as small in other situations [e.g., as pointed out in Ref. [54] for the SXS: BBH:0004 data set, $(q,\chi_1,\chi_2) = (1,-0.50,0)$]. In principle, we think that a careful analysis of the (hopefully very small) impact of the CoM drifts on all the EOB/NR comparisons discussed in this paper, both for phasing and energetics, will be needed in the future.

2. Computation of $E_b(j)$ from SXS waveform data

Let us now turn to explaining how $E_b(j)$ curves are computed in practice. First of all, we need to identify the initial state of the system, i.e. the initial $(J^0_{\rm ADM}, M^0_{\rm ADM})$. For each simulation, this information is provided in the file `metadata.txt` that is found in any of the `Lev*` directories that can be downloaded at `http://www.black-holes.org/waveforms/` for any given configuration. Then, the next step is to take all multipoles up to $\ell = 8$ and use them to compute the fluxes of energy and angular momentum as functions of time. In inspecting them, one quickly realizes that all simulations basically split into two equivalence classes depending on the properties of the initial transient in the fluxes driven by the junk radiation: In class (A), one sees a huge burst of energy and angular momentum radiated during approximately the first $150M$ of evolution. This behavior is displayed in the top panel of Fig. 25, that refers to the $\chi_1 = \chi_2 = +0.98$ case. Once the total losses at time t are obtained (by integrating the fluxes up to time t), the presence of such a big burst of radiation results in a huge shift in the (j, E_b) plane away from $(J^0_{\rm ADM}, M^0_{\rm ADM})$. This raw curve is represented as a gray, dashed line in Fig. 25. The location of the merger is indicated by a filled, grey circle. The unphysical nature of the initial, junk-related, shift is indicated by the fact that the

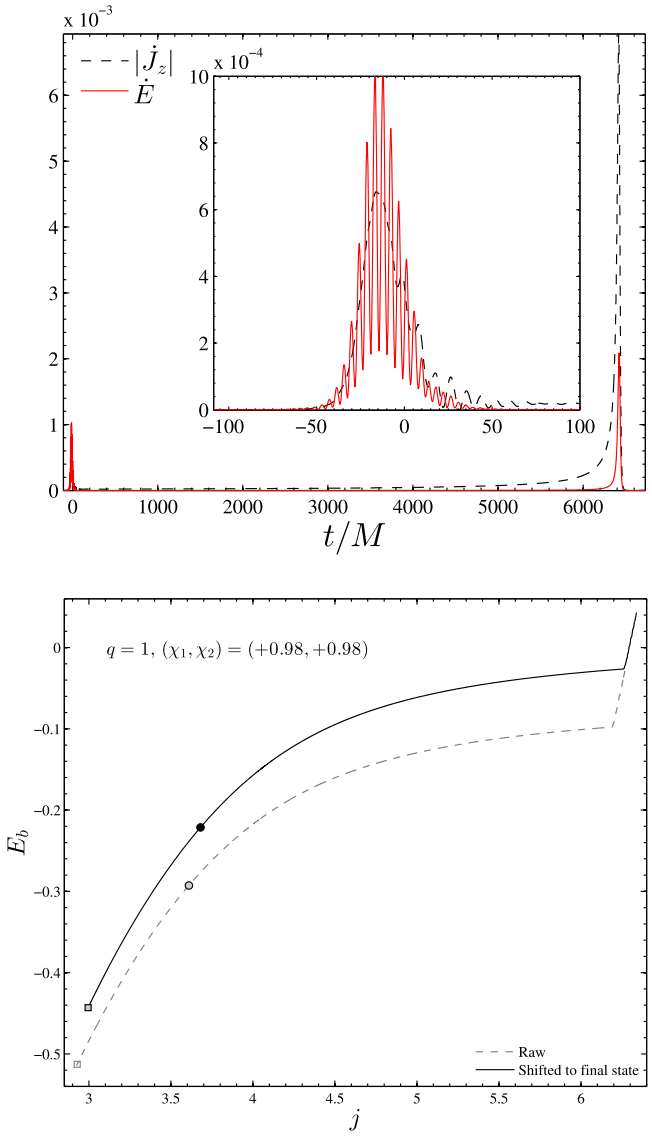

FIG. 25. Computation of $E_b(j)$ for $\chi_1 = \chi_2 = +0.98$. The huge burst of junk radiation (top panel) introduces a huge, unphysical, vectorial shift of the raw curve (grey, dashed), whose end point is strongly displaced from the actual final state (j_f, M_f) (grey square on the plot) given in the `metadata.txt` file of the SXS catalog. The solid curve is obtained by applying a shift vector $(\Delta j^0, \Delta E^0_b)$ to the raw curve so that the final point of the shifted $E_b(j)$ coincides with (j_f, M_f). The filled circles mark the merger location. See text for further details.

last point of the $E_b(j)$ curve, which should coincide, to a good approximation, with the mass and angular momentum of the final black hole (j_f, M_f), significantly differs from them.

The value of (j_f, M_f) is among the data given in the SXS catalog, and is notably included in the `metadata.txt` file. In Fig. 25, the actual (j_f, M_f) is represented by a filled, grey square on the plot, while the end point of the raw $E_b(j)$ curve (indicated by an empty square) is noticeably displaced from (j_f, M_f) due to the effect of the junk radiation. Such displacement should be corrected, as we shall discuss below. In the second class of data, that we call (B), such an unphysical initial burst of GW radiation is much smaller and the raw computation of the $E_b(j)$ curve gives a result that, without any additional shift, is visually consistent with the known final NR state. This is illustrated

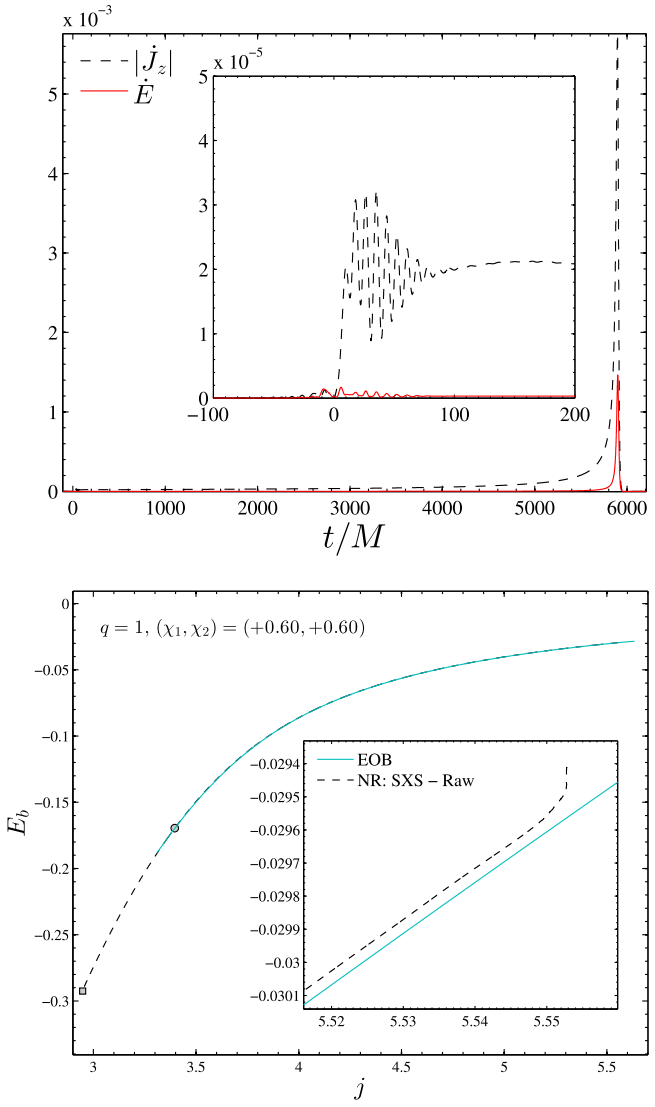

FIG. 26. Different phenomenology for $\chi_1 = \chi_2 = +0.60$. The initial burst of radiation is much more moderate than the $\chi = +0.98$ case so that the direct, raw computation of $E_b(j)$ looks already visually consistent with the final state and the EOB curve. Additional fine-tuning of $(\Delta j^0, \Delta E_b^0)$ is still allowed and it is then performed to further minimize the EOB/NR difference (within the NR uncertainty) for large values of j. See text for details.

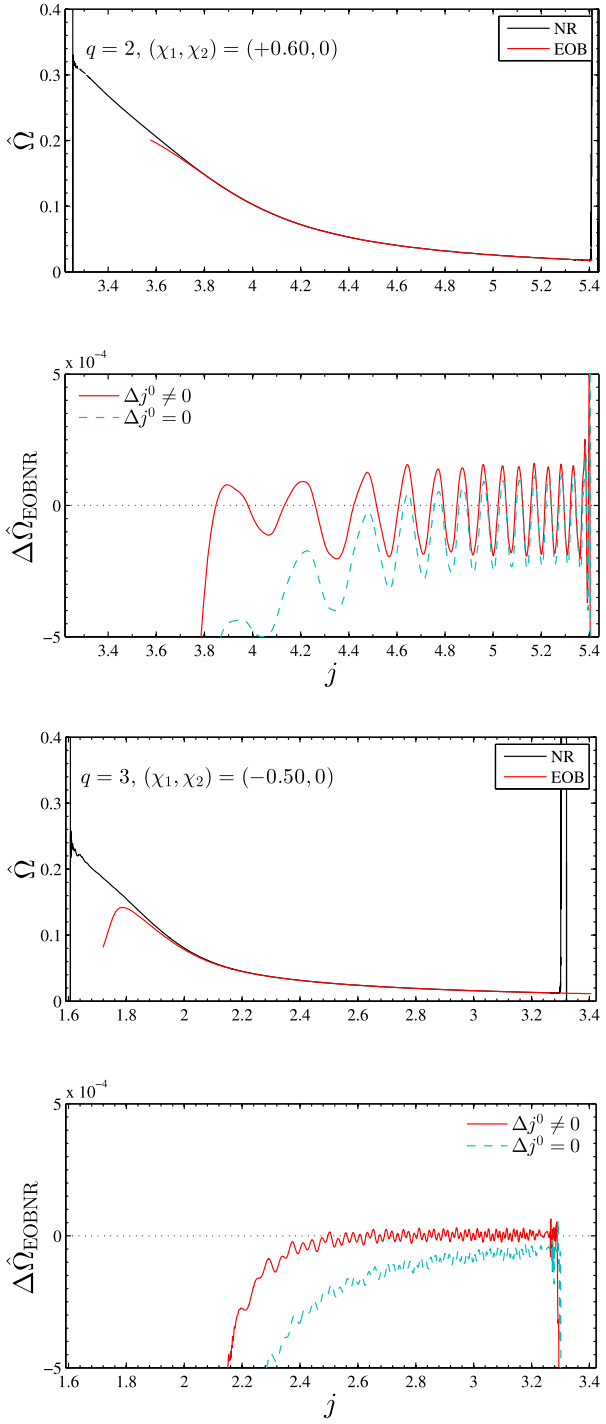

FIG. 27. Choosing Δj^0 by inspecting the EOB/NR differences between dimensionless orbital frequencies $\hat{\Omega}$ for two representative data sets. The bottom subpanel of each configuration illustrates how $\Delta\hat{\Omega}^{\rm EOBNR}$ is flattened (and the eccentricity-driven oscillation averages zero) on a large j interval once a good choice of Δj^0 is made.

for the case $\chi_1 = \chi_2 = +0.60$ in Fig. 26. Still (as highlighted in the inset of the figure) the NR curve, when zooming on the difference in the early part (see inset), exhibits a significant early deviation from the EOB, contrary to what was happening for the $\chi_1 = \chi_2 = +0.60$ case with Llama data, a simulation starting at a smaller value of j.

Finally, in both cases, (A) or (B), we need to apply a shift vector $(\Delta j^0, \Delta E_b^0)$, which will be larger in case (A). In a first step [which is mostly useful for case (A)] we apply a first shift $(\Delta j^f, \Delta E_b^f)$ allowing the final point of the $E_b(j)$ curve to essentially (within $\lesssim 10^{-4}$) coincide with (j_f, M_f). In a second step, we refine the determination of the vectorial shift by performing a second, smaller shift $(\Delta j^0, \Delta E_b^0)$.

The second shift vector, simply denoted $(\Delta j^0, \Delta E_b^0)$, is determined as follows. First of all we look at the dimensionless"orbital frequency" $\hat{\Omega} \equiv M\Omega$, that is defined (both in the EOB model and NR) as $\hat{\Omega} = \partial E_b / \partial j$. This quantity is, by construction, independent of the constant ΔE_b^0 but depends on Δj^0. We then compute the difference $\Delta\hat{\Omega}^{\rm EOBNR}(j) \equiv \hat{\Omega}^{\rm EOB}(j) - \hat{\Omega}^{\rm NR}(j)$ and plot it versus j. The shift Δj^0 is chosen so that $\Delta\hat{\Omega}(j)$ is "flattened" as much as possible on the largest possible j interval. In practice, we choose Δj^0 such that the oscillating (because of residual, tiny, eccentricity effects in the NR waveform) $\Delta\hat{\Omega}(j)$ averages to zero. Figure 27 shows the oscillating $\Delta\hat{\Omega}(j)$ for two, fiducial, configurations chosen randomly in the data sample: $(q, \chi_1, \chi_2) = (2, 0.6, 0)$ or $(q, \chi_1, \chi_2) = (3, -0.50, 0)$. In both cases, the raw $\Delta\hat{\Omega}$ (blue line) shows a trend that can be flattened by just choosing properly the constant Δj_0 (red curve). Once this is done, we inspect the difference $\Delta E_b^{\rm EOBNR} = E_b^{\rm EOB} - E_b^{\rm NR}$ and we find it remains practically constant on a large j interval. We then choose ΔE_b^0 so that the $\Delta E_b^{\rm EOBNR}$ is found to oscillate around zero. This algorithm for determining the shift vector $(\Delta j_0, \Delta E_b^0)$ can be applied to all SXS spin-aligned configurations at our disposal. Note that the shifts that are so determined are, in most cases, tiny but relevant on this scale. In some cases [see e.g. case $(q, \chi_1, \chi_2) = (8, -0.5, 0)$ in Fig. 14] the combination of the two shifts leads to an end point for the shifted $E_b(j)$ NR curve that is close to, but visibly displaced with respect to the (j_f, M_f) provided in the `metadata.txt`. Note however that in this case the total angular momentum changes sign during the inspiral which may be connected to subtleties in the computation of $E_b(j)$. We leave to future work a deeper investigation of this and similar cases.

For completeness, we list in Table III the shift vectors $(\Delta j^0, \Delta E_b^0)$ that are used to improve the compatibility between $(\Delta j^0, \Delta E_b^0)$ the NR $E_b(j)$ and the EOB one. The numbers listed in the table always indicate the crucial "second-shift" vector mentioned above [i.e., are applied to curves already shifted by $(\Delta j^f, \Delta E_b^f)$ so as the final point of $E_b(j)$ approximately coincides with (j_f, M_f)], except for those data sets marked by an asterisk, where $(\Delta j^0, \Delta E_b^0)$ is applied directly to the raw data.

[1] T. Damour and A. Nagar, Phys. Rev. D **90**, 044018 (2014).
[2] T. Damour, Phys. Rev. D **64**, 124013 (2001).
[3] A. Buonanno, Y. Chen, and T. Damour, Phys. Rev. D **74**, 104005 (2006).
[4] T. Damour, P. Jaranowski, and G. Schaefer, Phys. Rev. D **78**, 024009 (2008).
[5] E. Barausse and A. Buonanno, Phys. Rev. D **81**, 084024 (2010).
[6] Y. Pan, A. Buonanno, L. T. Buchman, T. Chu, L. E. Kidder, H. P. Pfeiffer, and M. A. Scheel, Phys. Rev. D **81**, 084041 (2010).
[7] A. Nagar, Phys. Rev. D **84**, 084028 (2011).
[8] E. Barausse and A. Buonanno, Phys. Rev. D **84**, 104027 (2011).
[9] Y. Pan, A. Buonanno, M. Boyle, L. T. Buchman, L. E. Kidder, H. P. Pfeiffer, and M. A. Scheel, Phys. Rev. D **84**, 124052 (2011).
[10] A. Taracchini, Y. Pan, A. Buonanno, E. Barausse, M. Boyle, T. Chu, G. Lovelace, H. P. Pfeiffer, and M. A. Scheel, Phys. Rev. D **86**, 024011 (2012).
[11] A. Taracchini, A. Buonanno, Y. Pan, T. Hinderer, M. Boyle *et al.*, Phys. Rev. D **89**, 061502 (2014).
[12] S. Balmelli and P. Jetzer, Phys. Rev. D **87**, 124036 (2013).
[13] S. Balmelli and P. Jetzer, Phys. Rev. D **91**, 064011 (2015).
[14] T. Damour and A. Nagar, Phys. Rev. D **90**, 024054 (2014).
[15] http://www.black-holes.org/waveforms.
[16] T. Chu, H. P. Pfeiffer, and M. A. Scheel, Phys. Rev. D **80**, 124051 (2009).
[17] G. Lovelace, M. Scheel, and B. Szilagyi, Phys. Rev. D **83**, 024010 (2011).
[18] G. Lovelace, M. Boyle, M. A. Scheel, and B. Szilagyi, Classical Quantum Gravity **29**, 045003 (2012).
[19] L. T. Buchman, H. P. Pfeiffer, M. A. Scheel, and B. Szilagyi, Phys. Rev. D **86**, 084033 (2012).
[20] A. H. Mroue and H. P. Pfeiffer, arXiv:1210.2958.
[21] A. H. Mroue, M. A. Scheel, B. Szilagyi, H. P. Pfeiffer, M. Boyle *et al.*, Phys. Rev. Lett. **111**, 241104 (2013).
[22] D. A. Hemberger, G. Lovelace, T. J. Loredo, L. E. Kidder, M. A. Scheel, B. Szilágyi, N. W. Taylor, and S. A. Teukolsky, Phys. Rev. D **88**, 064014 (2013).

[23] G. Lovelace, M. A. Scheel, R. Owen, M. Giesler, R. Katebi *et al.*, Classical Quantum Gravity **32**, 065007 (2015).
[24] M. A. Scheel, M. Giesler, D. A. Hemberger, G. Lovelace, K. Kuper, M. Boyle, B. Szilágyi, and L. E. Kidder, Classical Quantum Gravity **32**, 105009 (2015).
[25] J. Blackman, S. E. Field, C. R. Galley, B. Szilágyi, M. A. Scheel, M. Tiglio, and D. A. Hemberger, Phys. Rev. Lett. **115**, 121102 (2015).
[26] T. Damour, A. Nagar, D. Pollney, and C. Reisswig, Phys. Rev. Lett. **108**, 131101 (2012).
[27] N. W. Taylor, M. Boyle, C. Reisswig, M. A. Scheel, T. Chu, L. E. Kidder, and Béla Szilágyi, Phys. Rev. D **88**, 124010 (2013).
[28] M. Boyle and A. H. Mroue, Phys. Rev. D **80**, 124045 (2009).
[29] T. Damour, A. Nagar, and S. Bernuzzi, Phys. Rev. D **87**, 084035 (2013).
[30] D. Pollney and C. Reisswig, Astrophys. J. **732**, L13 (2011).
[31] C. Reisswig, N. T. Bishop, D. Pollney, and B. Szilágyi, Phys. Rev. Lett. **103**, 221101 (2009).
[32] N. T. Bishop, R. Gomez, L. Lehner, and J. Winicour, Phys. Rev. D **54**, 6153 (1996).
[33] D. Bini and T. Damour, Phys. Rev. D **87**, 121501 (2013).
[34] T. Damour, P. Jaranowski, and G. Schfer, Phys. Rev. D **91**, 084024 (2015).
[35] A. Buonanno and T. Damour, Phys. Rev. D **62**, 064015 (2000).
[36] T. Damour and A. Nagar, Phys. Rev. D **79**, 081503 (2009).
[37] S. Bernuzzi, A. Nagar, T. Dietrich, and T. Damour, Phys. Rev. Lett. **114**, 161103 (2015).
[38] S. Bernuzzi, A. Nagar, M. Thierfelder, and B. Brugmann, Phys. Rev. D **86**, 044030 (2012).
[39] C. Reisswig and D. Pollney, Classical Quantum Gravity **28**, 195015 (2011).
[40] D. Pollney, C. Reisswig, E. Schnetter, N. Dorband, and P/ Diener, Phys. Rev. D **83**, 044045 (2011).
[41] C. Reisswig, R. Haas, C. D. Ott, E. Abdikamalov, P. Mösta, D. Pollney, and E. Schnetter, Phys. Rev. D **87**, 064023 (2013).
[42] D. Bini and T. Damour, Phys. Rev. D **86**, 124012 (2012).
[43] T. Damour, P. Jaranowski, and G. Schaefer, Phys. Rev. D **89**, 064058 (2014).
[44] M. Levi and J. Steinhoff, J. Cosmol. Astropart. Phys. 12 (2014) 003.
[45] B. R. Iyer and C. Will, Phys. Rev. D **52**, 6882 (1995).
[46] T. Damour, A. Nagar, and L. Villain, Phys. Rev. D **89**, 024031 (2014).
[47] D. Shoemaker, https://dcc.ligo.org/cgi-bin/DocDB/ShowDocument?docid=2974.
[48] Y. Pan, A. Buonanno, A. Taracchini, M. Boyle, L. E. Kidder, A. H. Mroué, H. P. Pfeiffer, M. A. Scheel, B. Szilágyi, and A. Zenginoglu, Phys. Rev. D **89**, 061501 (2014).
[49] B. Szilgyi, J. Blackman, A. Buonanno, A. Taracchini, H. P. Pfeiffer, M. A. Scheel, T. Chu, L. E. Kidder, and Y. Pan, Phys. Rev. Lett. **115**, 031102 (2015).
[50] S. Husa, S. Khan, M. Hannam, M. Prrer, F. Ohme, X. J. Forteza, and A. Boh, Phys. Rev. D **93**, 044006 (2016).
[51] C. Reisswig, N. T. Bishop, D. Pollney, and B. Szilágyi, Classical Quantum Gravity **27**, 075014 (2010).
[52] T. Damour, E. Gourgoulhon, and P. Grandclement, Phys. Rev. D **66**, 024007 (2002).
[53] S. Bernuzzi, T. Dietrich, W. Tichy, and B. Bruegmann, Phys. Rev. D **89**, 104021 (2014).
[54] M. Boyle, arXiv:1509.00862.
[55] S. Ossokine, F. Foucart, H. P. Pfeiffer, M. Boyle, and B. Szilgyi, arXiv:1506.01689.